PPPL-2165

DR-06572

PPPL-2165

UC20-F

I-18440

STUDIES OF ENERGETIC ION CONFINEMENT DURING FISHBONE EVENTS IN PDX

By

J.D. Strachan, B. Grek, W. Heidbrink, D. Johnson, S. Kaye, H. Kugel, B. LeBlanc, and K. McGuire

NOVEMBER 1984

PLASMA PHYSICS LABORATORY

PRINCETON UNIVERSITY

PRINCETON, NEW JERSEY

PREPARED FOR THE U.S. DEPARTMENT OF ENERGY, UNDER CONTRACT DE-AC02-76-CHO-3073.

STUDIES OF ENERGETIC ION CONFINEMENT DURING FISHBONE EVENTS IN PDX

J.D. Strachan, E. Grek, W. Heidbrink, D. Johnson, S. Kaye,
H. Kugel, B. LeBlanc, and K. McGuire

Plasma Physics Laboratory
Princeton University
P. O. Box 451
Princeton, NJ 08544 USA

PPPL--2165
DE85 004399

ABSTRACT

The 2.5-MeV neutron emission from the beam-target $d(d,n,)^3He$ fusion reaction has been examined for all PDX deuterium plasmas which were heated by deuterium neutral beams. The magnitude of the emission was found to scale classically and increase with $T_e^{3/2}$ as expected when electron drag is the primary energy degradation mechanism. The time evolution of the neutron emission through fishbone events was measured and used to determine the confinement properties of the energetic beam ions. Many of the experimental results are predicted by the Mode Particle Pumping theory.

1. INTRODUCTION

High beta operation on PDX exhibited a new instability called the fishbone instability[1,2]. This instability was thought to be a large n=1, m=1 internal kink mode which, due to the plasma outshift at large poloidal beta, also excited n=1, m=2,3,4 MHD modes. These MHD modes were correlated with a loss of energetic injected beam ions. In its most violent form, the fishbone instability could significantly reduce the flow of beam power to the plasma. The fishbone instability has been identified as one cause of beta saturation on PDX[1].

In this paper, the influence of the fishbone events on the energetic ion confinement is inferred from neutron measurements on PDX. Previous PDX reports using the $d(d,n)^3He$ reaction were limited to deuterium neutral beam injection into hydrogen plasmas ($D^\circ \rightarrow H^+$)[1,2]. A major uncertainty in the interpretation of neutron data from those plasmas is that the relative concentration of hydrogen and deuterium in the plasma is not well known, making it difficult to evaluate the relative importance of beam-beam and beam-target reactions. Further, the relative importance of beam-beam reactions is higher during $D^\circ \rightarrow H^+$ injection. In this paper, we examine all the available PDX data during $D^\circ \rightarrow D^+$ injection. The major aim is to provide quantitative values of the energetic-ion confinement time during fishbone events and to relate that confinement to other plasma parameters. The average and instantaneous confinement of the energetic beam ions can be described by the time evolution of the 2.5-MeV neutron emission from the beam-target $d(d,n)^3He$ reactions. We find that the instantaneous energetic-ion loss rate is proportional to the magnitude of the MHD oscillation ($\tilde{B}\theta/B\theta$), as is predicted by the Mode Particle Pumping Theory of R. White et al[3]. Also the average energetic ion confinement decreases when the product of toroidal beta and

safety factor, βq, increases in qualitative agreement with the expectations of pressure-driven kink modes[1].

2. EXPERIMENT

2.A NEUTRON DIAGNOSTICS:

The measurements reported here were made using the 2.5-MeV neutron emission from the $d(d,n)^3He$ fusion reaction. These detector systems have been described previously[4] and their operation will only be briefly summarized here.

1. The slow time evolution and absolute magnitude of the 2.5-MeV neutron emission were detected by an array of moderated neutron detectors with 10 msec time resolution[4]. The absolute calibration was achieved using Indium activation foils[5] placed on the PDX vessel. The accuracy of the measurement of the absolute emission level is probably about a factor of 1.5 including both systematic calibration uncertainties and counting statistics.
2. High frequency oscillations of the 2.5-MeV neutron emission were detected with an array of plastic NE102A and NE451 ZnS scintillators placed close to the vacuum vessel and connected by light pipes to photomultipliers[4]. The intrinsic detector frequency response is of the order of 1 MHz. In practice, the frequency response is limited by counting statistics to about 100-kHz resolution of a few percent neutron oscillations at emission levels of $10^{14}sec^{-1}$. In order to detect any possible contamination of the scintillator signal by hard X-rays, a NaI detector was used to measure hard X-rays produced by runaway electrons leaving the plasma. It was found that bursts of

hard X-rays occurred during Hα spikes but not during fishbones (except when Hα spikes occurred simultaneously with the fishbones).

2.B *INTERPRETATION*

For the PDX plasmas with $D^0 \rightarrow D^+$ neutral beam injection, the beam-target fusion reactions typically make up 75% of the total emission. The beam-beam reactions make up the remaining emission and the thermonuclear rates are unimportant (see Sec. 3.A)). Insofar as the fusion emission can be described by beam-induced reactions, there are particularly simple relationships which relate the fusion emission to the confinement of energetic injected ions. For example, the rate of decay of the $d(d,n)^3He$ rate during the fishbone yields the instantaneous confinement time, τ_B, of the most energetic of the injected ions.

For beam-target fusion reactions, the reaction rate, I, is approximately the product of the target deuterium density, n, the number of energetic ions, N, and the fusion reactivity σv evaluated at the energetic ion energy, W[4].

$$I = nN\,(\sigma v)\Big]_W. \qquad (1)$$

The quantity N represents the cross-section weighted energetic ion number

$$N \equiv \int\int f_b(r,\bar{v})\sigma\bar{v}\; d\bar{v}\; dr/(\sigma v)\Big|_W,$$

where f_b is the beam distribution function and the integral is over the plasma volume. The dominant contribution to N is from the portion of velocity space that is close to the full energy component of the neutral beam injection energy and pitch angle.

The energetic ion population changes in time due to the injection of additional beam ions at a source rate, S, and due to the loss of energetic ions through thermalization or transport. It is convenient to consider separately the loss rate in the absence of fishbones, τ_n^{-1}, which is classically due to electron drag, and the losses during fishbones, which we characterize by a confinement time τ_B. The rate of change of the energetic ion population, $\dot{N}$, is

$$\dot{N} = S - N/\tau_n - N/\tau_B. \qquad (2)$$

We can solve Equations (1) and (2) to determine the evolution of the instantaneous confinement time $\tau_B(t)$ as

$$\tau_B(t) = \frac{I(t)}{I(t_o) - I(t)}, \qquad (3)$$

where t_o is a time prior to the onset of the fishbone instability such that $I(t_o) = I(t)$ and

$$\dot{N}(t_o) = S(t) - N(t)/\tau_n(t). \qquad (4)$$

This means that using Eq. (3), one can determine the confinement time of the energetic (cross-section weighted) beam ions by simply measuring the decay rate of the neutron emission during the fishbone, the neutron intensity, and the buildup rate of the neutron emission in the absence of the fishbone but at the same neutron intensity (see Fig. 1). The only approximations are that the loss rate τ_n^{-1}, the beam injection voltage, W, the source rate, S, and the deuterium target density, n, do not change between t_o and t. Since the loss rate in the absence of fishbones is dominated by electron drag, these are all reasonable approximations.

The contribution of the beam-beam reactions to the total neutron emission is typically ~ 0.25 (see Sec. 3.A). If we consider a neutron emission composed of both beam-beam and beam-target emissions, then Equation (1) becomes

$$I = I_{BT} + I_{BB}, \text{ where } I_{BT} \propto N \qquad (1A)$$

$$\text{and approximately } I_{BB} \propto N^2.$$

If we define ε as the ratio of beam-beam reactions to beam-target reactions $\varepsilon = I_{BB}/I_{BT}$, then the derivation proceeds as before with a slightly different derived energetic ion confinement time, τ_B^*

$$\tau_B^* \simeq \tau_B \left(\frac{1 + 2\varepsilon}{1 + \varepsilon} \right), \qquad (3A)$$

where τ_B remains defined by Eq. (3). This means that if all the reactions were beam-beam rather than beam-target, we would be underestimating the energetic ion confinement time by a factor of two by using Eq. (3). For the PDX plasmas, ε is in the range of 0.2 + 0.5, indicating that use of Eq. (3) can underestimate the energetic ion confinement time by about 20% to 30%.

One can also define an average energetic ion confinement time $\langle \tau_B \rangle$ from the magnitude of the reaction drop at each fishbone, $\Delta I/I$, and the period between fishbones event, P_{fb}

$$\langle \tau_B \rangle = \frac{P_{fb}}{\ell n \left(1/(1 - \Delta I/I)\right)} . \qquad (5)$$

This average confinement time is approximately the inverse of the energetic ion loss rate $\nu_{LOSS} = 1/\langle \tau_B \rangle$ defined in Ref. [1].

2.C DESCRIPTION OF PLASMAS

The data here represent all the available PDX neutron data during $D^0 \rightarrow D^+$ neutral beam operation. (B_ϕ = 10 → 22 kG, I_ϕ = 150 → 500 kA, P_B = 1 → 5 MW, a = 0.4 m, R = 1.4 m). This operation occurred to a large extent during the last half year of PDX and consisted almost entirely of diverted plasmas. The run objective during this time was usually (but not exclusively) the study of H-modes[6].

1) We established a data base where the absolute value of the neutron emission was related to the TV Thomson Scattering profiles. The data were gathered during the quasisteady positions of the beam injection and were selected if there were relatively small error bars on $T_e(r)$ and $n_e(r)$. All available $D^0 \rightarrow D^+$ data were examined.

2) We established a data base where the minimum instantaneous beam ion confinement time, τ_B was related to the signal of a Mirnov coil [7] mounted near the outer wall of the vacuum vessel ($\tilde{B}_\theta/B_\theta$ amplitude, frequency, growth rate, etc.). All the observed fishbone events during $D^0 \rightarrow D^+$ having fast digitization (1 or 2 μsec) of the neutron signal were examined.

3) We established a data base where the time evolution of the neutron emission was recorded throughout the neutral beam heating and related to the deduced average beam ion confinement time, $\langle \tau_B \rangle$, and to the β values determined from the plasma equilibrium [1]. The accumulation of this data is primarily limited by the occurrence of neutron signal digitization for a time duration sufficient to see the fishbone period. (The neutron signal was digitized with the MHD Mirnov signals which featured a fast digitization time of 1 μsec for 6 msec, of 2 μsec for 12 msec, etc.). All available $D^0 \rightarrow D^+$ data were

examined and included if neutron drops or Mirnov MHD bursts could be seen.

3. RESULTS

3.A ABSOLUTE NEUTRON EMISSION LEVELS

A data base was formed of all the $D^0 \rightarrow D^+$ absolute neutron emission levels for which $n_e(r)$ and $T_e(r)$ data [from TV Thomson Scattering] also existed. The electron profile data are required to specify the electron drag on the energetic ions.

Experimentally, the dominant scaling of the neutron emission, I, is

$$I \propto T_e^{1.5} P_B n^{0.5} \text{ at constant } W_B \qquad (6)$$

where T_e is the central electron temperature, P_B is the applied beam power, n is the volume-averaged density, and W_B is the average beam voltage.
A good fit ($R^2 = 0.83$) is also attained (Fig. 2) with

$$I \propto T_e^{3/2} P_B n^{1/2} W_B^2 \qquad (7)$$

and the scaling holds over about two orders of magnitude in neutron emission. The correlation coefficient R^2 is the relative reduction in the standard deviation obtained by making the fit.

If a confined beam ion slows down due to electron drag, then due to the strong dependence of the fusion reaction cross section on energy, a typical beam ion has an appreciable probability of undergoing a fusion reaction for a

time $\tau_n \approx \tau_s/3$, where τ_n is the cross-section weighted slowing-down time, and τ_s is the total slowing-down duration. If most of the injected beam ions are confined for a time long compared to the slowing-down time ($\tau_n << \langle\tau_B\rangle$), then the number of energetic beam ions in the hot plasma core is approximately [4]

$$N = \xi \dot{N}_B \tau_n \qquad (8)$$

where ξ is the fraction of the injected beam ions captured in the central plasma regions, and $\dot{N}_B$ is the injection rate of the full energy component of the beam ions. For electron drag, $\tau_n \propto T_e^{3/2}/n_e$, and for $Z = 1$ deuterium plasmas, one expects

$$I \propto \xi T_e^{3/2} P_B W_B^2. \qquad (9)$$

Interestingly, the scaling of the neutron emission with the electron drag ($T_e^{3/2}$) is the single strongest scaling observed in the data (Fig. 3). Saturation of the neutron emission at the highest beam powers is possible but cannot be definitely concluded due to the small number of high power data points (Fig. 2).

The scaling of neutron emission, I, with beam voltage is difficult to observe on the particular set of data available from PDX. The observed density dependence [Eq. (6)] (Fig. 4a) is possibly due to the penetration factor, ξ, and is likely a combination of shine-through (reducing the absorbed power) and increased beam-ion charge-exchange losses at the lower densities. The density scaling can also be expressed as a neutral mean-free path, l, scaling (Fig. 4b). It is also likely that the ratio n_d/n_e increases with electron density (due to a probable decrease in Z_{eff}), which might also contribute to the density dependence of Fig. 4.

For a reduced set of the available PDX data, TRANSP runs [8] have also been made which predict the absolute neutron emission and which calculate the beam-target, beam-beam, and thermonuclear neutron emission levels. The agreement between TRANSP and the experimental values (Fig. 5) is good. TRANSP calculates that the beam-target reactions are ~ 75% of the total emission, with the remainder due to beam-beam reactions.

Essentially, the dominant empirical scaling of the neutron emission magnitude during $D^0 \rightarrow D^+$ corresponds to that expected for classical behaviour of beam-target fusion reactions. Apparently, the fishbone instability does not have a strong effect on the magnitude of the emission. This is expected if $\langle \tau_B \rangle \gg \tau_n$. However, at any one condition, there is still a large amount of scatter which could hide significant (~ 50%) reductions in the neutron emission due to the fishbone activity. It should be stressed, again, that we are discussing here the neutron emission values averaged over 10 msec periods and not the obvious 30% drops in the neutron emission observed for short times at the fishbone instability (e.g., Fig. 1).

3.B INSTANTANEOUS CONFINEMENT TIMES, τ_B

Energetic ion losses were observed with four types of events:

1) the classic fishbone with $\tilde{B}\theta/B\theta$ oscillating only in the range $10 \rightarrow 20$ kHZ [2],
2) a high frequency event with $\tilde{B}\theta/B\theta$ oscillating only in the range of $50 \rightarrow 100$ kHZ,
3) a double frequency event with $\tilde{B}\theta/B\theta$ oscillating both in the frequency range of $10 \rightarrow 20$ kHZ as well as in a frequency range approximately $4 \rightarrow 6$ times higher, and

4) a sawtooth event with $\tilde{B}\theta/B\theta$ oscillating in the range of 4 + 10 kHZ. Sawtooth events with $\tilde{B}\theta/B\theta$ oscillating at higher frequencies were not observed in the present data set.

Observations from each of these events will be described separately. In previous PDX publications, fishbones are considered to be only those events where a 10 + 20-kHZ oscillation is observed. Here we examined all events where the MHD signal is coupled to the plasma edge so that an oscillating signal is seen on the Mirnov coils. Often an energetic ion loss is inferred from the neutron emission for these events.

3.B-1 SINGLE FREQUENCY FISHBONES

If we examine the time evolution of a 20-kHz fishbone event (Fig. 1) then we see that $\tilde{B}\theta/B\theta$ grows and falls exponentially (Fig. 6). The neutron emission rises before the fishbone while the magnetic oscillation at the edge of the plasma is small. The neutron signal begins decaying when the amplitude of the magnetic oscillation is near its maximum and, as it decays, it also exhibits the approximately 20-kHZ internal fishbone oscillations with an amplitude $\tilde{I}/I \approx 5\%$. During the fishbone event in Fig. 1, the frequency of the magnetic oscillation decayed (Fig. 6) from 22 kHZ to approximately 11 kHZ. The instantaneous confinement time of the energetic beam ions as determined from the decay rate of the neutron emission, using Eq. (3), falls exponentially (Fig. 6) to about 1 msec and rises as the magnetic oscillation decreases. The influence of the 20-kHz neutron oscillation was ignored in deducing the neutron decay rate.

A strong correlation ($R^2 = 0.96$) (Fig. 7) exists between the instantaneous confinement time, τ_B, [obtained using Eq. (3)] and the magnitude of the magnetic oscillation through the fishbone event of Fig. 1.

$$\tau_B = 2.9 \times 10^{-5} \left(\frac{\tilde{B}\theta}{B\theta}\right)^{-0.83} \qquad (10)$$

A data base was formed of all available $D^\circ \rightarrow D^+$ fishbone events and the peak $\tilde{B}\theta/B\theta$ was recorded as well as the magnetic oscillation frequency (at the peak neutron decay, before the neutron decay, and after the neutron decay) and the neutron decay rate at the peak $\tilde{B}\theta/B\theta$. In Fig. 8 are plotted the range of $\tilde{B}\theta/B\theta$ values and the frequency, at the peak neutron decay, F, for the single frequency fishbone events. The solid points are events which did not have an observable (0.2%) drop in neutron emission associated with the magnetic oscillation. Evidently, there is an approximate threshhold for observable loss of energetic ions of

$$\frac{\tilde{B}\theta}{B\theta} \gtrsim 10^{-3} .$$

Examining all the events indicates roughly that (Fig. 9)

$$\tau_B = 7.1 \times 10^{-6} \left(\frac{\tilde{B}\theta}{B\theta}\right)^{-1.3} \qquad (11)$$

with a high correlation coefficient ($R^2 = 0.83$). The magnitude of the neutron drop ($\Delta I/I$), which is roughly the fraction of energetic beam ions lost during the fishbone event, is correlated with the minimum instantaneous confinement time, τ_B, and with the magnitude of the neutron oscillation at the fishbone frequency ($\tilde{I}/I$) (Fig. 10).

The amount that the frequency decreased during the fishbone (ΔF = the difference between the initial frequency before the neutron decays and the final frequency after the neutron decay has ended) depended on the initial frequency, F_i, and the eventual maximum size of the magnetic oscillation (Fig. 11) scaling as

$$\Delta F = 0.026\, F_i^2 \left(\frac{\tilde{B}\theta}{B\theta}\right)^{0.25} . \qquad (12)$$

Since the $\tilde{B}\theta/B\theta$ values cover such a wide range of values, both F_i and $\tilde{B}\theta/B\theta$ are about equally important in the variation of ΔF in Eq. (12). Since there is a threshold in $\tilde{B}\theta/B\theta$ before there is a significant (measurable) loss of energetic ions (Fig. 8), this means that there is a noticeable decrease in the frequency even if there is no observable loss of energetic ions.

In principle, placement of collimated scintillators poloidally and toroidally around the PDX plasma could allow the poloidal and toroidal structure of the neutron oscillation at the internal fishbone frequency to be determined. However, due to the limited diagnostic access to PDX, massive neutron collimators could not be used and only limited toroidal and polodial phase information was obtained. Nonetheless, it should be realized that an uncollimated detector views only a small portion of the plasma immediately in front of the detector. The toroidal resolving angle (half width of detector sensitivity) is about 45° [9].

The phase information we obtained is consistent with the interpretation that the neutron emitting region inside the plasma has the same n=1, m=1 structure that the central soft X-ray emission exhibits, implying that the neutron fluctuation, $\tilde{I}$, arises primarily from the movement towards and away from the detector of the neutron-emitting region of the plasma. Using the expression for the neutron emission from a toroidal line source [6] indicates that the magnitude of the neutron fluctuation, $\tilde{I}$, is linearly related to the radial extent of the plasma motion (Fig. 12), with a 5% neutron oscillation corresponding to a plasma motion of about 7 cm. Measurement of the motion of the soft X-ray hot spot indicates that the magnitude of the neutron

fluctuation (Fig. 13) can be explained by the magnitude of the central plasma in-out motion. The phase is such that the neutron fluctuation has a peak when the X-ray hot spot is outshifted (i.e., the hot region of the plasma is closest to the neutron detector). Evidently, the energetic ion population forms the same spatial structure as the electrons in response to the MHD mode.

Some toroidal phase information was obtained by comparing the signal of two scintillators displaced toroidally by 180° but mounted at the same poloidal position (horizontal midplane). The detectors signals were out of phase (Fig. 14) indicating that the neutron signal had an n = odd structure consistent with the n = 1 structure of the MHD mode.

Some poloidal phase information was obtained by comparing the signal of two scintillators displaced poloidally by about 60° but at the same toroidal location. The detector signals had a phase lag consistent with motion in the ion diamagnetic direction and the signals could be simulated in phase and magnitude by an m = 1 rotating structure of the neutron emitting toroidal line source (Fig. 15). This poloidal information rules out the possibility that the neutron fluctuation could be caused by an outwardly propagating beacon of energetic ions [3] moving in phase with the n = 1, m = 1 internal mode. It should be emphasized that we are not ruling out the existence of such a beacon but only that the beacon did not cause the 20-kHz neutron fluctuation. A neutron fluctuation caused by an outwardly moving beacon of energetic ions is a possibility since these ions are closer to the detectors and since the high ion energies observed [10] would significantly increase the fusion reactivity of some of the escaping ions.

Due to the statistical fluctuations, we cannot eliminate the possibility that some substructure might exist on the 20-kHz neutron fluctuation (e.g., Fig. 14a). On many occasions, there is little or no substructure (e.g., Fig.

13b). The identification of the neutron fluctuation as a plasma in-out motion and the observed correlation of the magnitude of the neutron drop with the neutron fluctuation amplitude can also be interpreted as a correlation of the instantaneous confinment time with the size, Δ, of the in-out motion (Fig. 16). Approximately

$$\tau_B \propto \Delta^{-2}. \qquad (13)$$

Alternatively, the same observation of the correlation of the magnitude of the neutron drop with the neutron fluctuation amplitude can be interpreted as a correlation with the ability of the energetic ions to redistribute into the spatial structure of the MHD mode.

3.B-2 HIGH FREQUENCY EVENT

Occasionally, events occur with a single frequency which is usually higher than the normal fishbone frequency by roughly a factor of five. These events may not truly be related to the ~ 20-kHz fishbone events, however, they also experience a loss of energetic ions. Of themselves, these events happen quite infrequently and without large drops in the neutron emission. However, quite often events occur with both high and low frequencies. In order to throw more light on the double frequency events, we first examine the single high frequency event.

The largest of these high frequency events (Fig. 17) has many similarities with the 20-kHz fishbones. The neutron emission drops as the magnetic oscillation reaches its peak and the frequency slows down considerably (Fig. 18) as the energetic ions are lost (from 90-kHz to 65-kHz in this case). The magnetic perturbation at the Mirnov coil is much smaller

($\sim 10^{-4}$), which probably indicates that the coupling of these oscillations from the plasma edge to the Mirnov coil is poorer than for the 20-kHz oscillations, as might be expected for higher m modes.

As for the low frequency events (Fig. 6), the confinement time of the energetic beam ions also decays pronouncedly as the magnetic perturbation grows. A correlation of τ_B with $\tilde{B}_\theta/B_\theta$ (Fig. 18) is again observed. The neutron counting statistics were too poor to see if any oscillations at the 5% level occurred during these events.

3.B-3 DOUBLE FREQUENCY FISHBONES

Often fishbone events have both ~ 20-kHz magnetic oscillations and also the 4 ÷ 6 times higher frequency oscillation [2,11]. The higher frequency will often precede the lower frequency (Fig. 19 is a common example). Occasionally, however, the higher frequency will occur as a burst in the middle of the 20-kHz fishbone or the 20-kHz oscillation will occur as a burst in the middle of an otherwise exclusively high frequency event.

As occurs without the presence of the higher frequency, the approximately 20-kHz $\tilde{B}_\theta/B_\theta$ oscillation grows and decays nearly exponentially (Fig. 20) while its frequency slows down. The time evolution of the energetic ion confinement, τ_B, (Fig. 20) has two minima, corresponding to the sequential peaking of the higher and lower frequency magnetic perturbations. The experimental confinement time is approximately the linear combination of the empirically scaled confinement times for the higher, τ_H, and lower, τ_L, frequency events.

$$\frac{1}{\tau_B} = \frac{1}{\tau_H} + \frac{1}{\tau_L} \qquad (14)$$

The peak energetic ion loss rate was examined for all the available $D^0 + D^+$ cases where the two frequencies were present and the loss rate was described by Eq. (14) (Fig. 21).

3.B-4 SAWTOOTH EVENTS

A small number of sawtooth events occurred which also involved a large reduction in neutron emission ($\Delta I/I \sim 20 + 30\%$), indicating a loss of energetic ions. These events differ from more usual sawtooth events since the MHD frequency is higher ($\approx$ 8-kHz) and the central n=1, m=1 MHD activity is coupled to the plasma edge and can be seen on the Mirnov coils (Fig. 23). In sawtooth events involving only internal redistribution of energetic ions without significant loss to the walls, the neutron intensity drops a small amount ($\Delta I/I \lesssim 3\%$) on a time scale of the cross-section weighted slowing down ($\tau_n \sim$ 3-5 msec) [4]. Larger drops on a faster time scale can indicate losses of energetic ions at the sawtooth as well as some probable internal redistribution.

In fact, the particle loss for these events is severe and occurs during a single MHD oscillation period (Fig. 22). The scaling of the energetic ion confinement time with the magnitude of the magnetic perturbation indicates (Fig. 23)

$$\tau_B \propto (\tilde{B}_\theta/B_\theta)^{-1/2}. \qquad (15)$$

3.C βq DEPENDENCE

For PDX limiter discharges [1], the marginal stability condition for pressure driven n = 1 internal kink modes is given by curves of constant βq ≈ 0.021, while the marginal stability condition for pressure driven n = ∞ internal kink modes (ballooning modes) is given by βq ≈ 0.05. β is the toroidal beta and q is the Shafranov value. These lines of marginal stability give only an indication of stability trends. Uncertainties in the actual q(r) and β(r) profiles make the lines uncertain and the ballooning mode calculations are probably the more uncertain of the two. We find (Fig. 24b) that the discharges with βq values above the n = 1 marginal stability curve do tend to have much larger average energetic ion losses. There exists a correlation ($R^2 \sim 0.6$) of the average energetic ion confinement with βq of the form

$$\langle \tau_B \rangle = 621(\beta q)^{-2.4} \qquad (16)$$

or

$$\langle \tau_B \rangle \approx (1.72 \times 10^{-3})^{-1} \exp.(-0.8\beta q), \qquad (17)$$

where these two scalings are indistinguishable due to the limited range of βq available (Fig. 25). The dependence of $\langle \tau_B \rangle$ on both β and q can be seen when the other parameter is held constant (Fig. 26).

For the present data, the scaling of $\langle \tau_B \rangle$ with βq is equivalent to a scaling of $\langle \tau_B \rangle \propto (B_\phi/P_B)^2$. Doing a regression analysis (Fig. 27) indicates that roughly

$$\langle \tau_B \rangle \propto B^3/\beta q^2 \qquad (18)$$

with a correlation coefficient of $R^2 = 0.72$. At constant βq ($0.3 < \beta q < 0.04$), $\langle \tau_B \rangle$ is dependent on B_ϕ with either (Fig. 28):

$$\langle T_B \rangle \cong 0.415\ e^{0.27 B_\phi}$$

or (19)

$$\langle T_B \rangle \cong 8.7 \times 10^{-4}\ B_\phi^{3.8}$$

having $R^2 = 0.77$ and 0.79, respectively.

Due to the particular data set available, the scaling with toroidal field is equivalent to a scaling with plasma current with approximately $\langle T_B \rangle \alpha\ I_\phi^{2.7}$ or $\langle T_B \rangle \alpha\ e^{0.56 I_\phi}$. Improved energetic ion confinement is expected in the Mode Particle Pumping theory [3] for reduced banana width or increase of plasma current, I_ϕ.

The amplitude of the fishbone event also depends on βq (Fig. 26). For the single frequency event (Sec. 3.B-1), the minimum instantaneous energetic ion confinement time T_B tends to be smaller when the plasma βq values are above the threshold for marginal stability [1] of the pressure driven kink mode (Fig. 24a). The high frequency events (Sec. 3.B-2) and double frequency events (Sec. 3-B.3) occurred in plasmas with parameters that were not noticeably different (Fig. 24c) than the plasmas in which the 20-kHz fishbone events occurred. No noticeable pattern distinguished the events where the higher or lower frequency dominated (Fig. 24c). As was the case for the single frequency events, there was a tendency for the most violent double frequency events to occur above the n=1 marginal stability line. The ratios of the two frequencies in the double frequency events tended to increase with βq (Fig. 29). The sawtooth events that involved losses of energetic ions (Sec. 3.B.4) occurred near the n=1 marginal stability curve (Fig. 24d).

4. DISCUSSION

4.A CLASSICAL NEUTRON EMISSION

The dominant empirical scalings of the magnitude of the neutron emission during $D^0 \rightarrow D^+$ correspond to that expected for classical behaviour of beam-target fusion reactions (Sec. 3.A). Apparently, for these PDX plasmas, the fishbone instability was not the dominant effect on the magnitude of the neutron emission. As described in Ref. [1], calculations of the gross energy confinement time indicate that fishbone losses do affect power deposition in the thermal plasma when the average energetic ion confinement time is reduced to about the beam ion slowing down duration ($\tau_S \simeq 15 \rightarrow 50$ msec for PDX conditions). These times become comparable for $\beta q \gtrsim 0.03$, a condition often achieved on PDX. The fishbone losses were not severe enough to reduce the average neutron emission rate seriously (i.e., more than about 50%, or the measurement uncertainty), since this requires that the average confinement time $\langle \tau_B \rangle$ be less than the cross-section weighted beam slowing-down duration τ_S (Sec. 2.B), and τ_n ($\tau_n \sim \tau_S/3$) was generally less than $\langle \tau_B \rangle$ (Fig. 25).

It is natural to compare the magnitude of the $D^0 \rightarrow D^+$ neutron emission to that obtained on PLT [4] since both machines used essentially the same set of neutron diagnostics calibrated in the same manner. Moreover, the beam voltages, plasma currents, plasma sizes, plasma densities, and temperatures were quite similar. The main differences are the higher toroidal field used on PLT, the larger beam powers available on PDX, and the perpendicular injection on PDX compared to the tangential injection on PLT.

Consistent with the findings of a nearly classical explanation of the absolute neutron emission for both PLT and PDX is the fact that the PLT tended to have relatively higher emission levels at lower densities and PDX tended to have relatively higher emission levels at higher densities. This difference

is expected to be due almost entirely to the difference in the injection angles: tangential injection concentrates the beam ion trapping on axis for very low densities while the perpendicular injection allows some ions to reach the plasma center at high plasma densities (Fig. 30).

4.B COMPARISON TO MODE PARTICLE PUMPING THEORY

R. White *et al.* [3] have described an energetic ion loss process caused by magnetic field distortions of the type that occur during the fishbone events. This "mode particle pumping" theory predicts a convective loss of energetic ions due to $\underline{E} \times \underline{B}$ drifts associated with the MHD mode. The loss is especially severe when the MHD frequency happens to equal the energetic ion precession frequency.

This minimum confinement time for the energetic ions can be written as roughly

$$\tau \simeq \frac{a}{2\dot{r}} \qquad (20)$$

where $\dot{r}$ is the average minor radial velocity of the most energetic ions given by Eq. (17) of Ref. 3

$$\langle \dot{r} \rangle \simeq \frac{R \cos(\delta)\, m\, \alpha_{nm}\, \omega_p J_0(m\theta_b)}{r\,(1 - \frac{nq}{m})} \qquad (21)$$

where $\cos(\delta) \sim 1/4$ is the phase between the mode and the particle

$m \simeq 3$

$1 - nq/m \simeq 1/2$

$J_0(m\theta_b) \simeq 1$ and θ_b is the bounce angle

$r \simeq a$

$\alpha_{nm} \propto (\tilde{B}_\theta/B_\theta)\ a^2/qR$

ω_p = precession frequency

being typical parameters for the illustrative case of Ref. [3], where the m=3 mode (caused by the outshifted n=1, m=1 central perturbation) is causing most of the energetic ion loss. Thus

$$\tau_{min} \propto \frac{q}{(\frac{\tilde{B}_\theta}{B_\theta})F} \qquad (22)$$

and the constant of proportionality is obtained from Fig. 4 of Ref. 3 which applies for a 0.5 msec MHD burst with $\tilde{B}_\theta/B_\theta$ of 1% as measured at the Mirnov coils (also the value used in our experimental comparisons, e.g., Fig. 6-8).

Comparison of the minimum loss time to the experimental values either through the fishbone of Fig. 1 (Fig. 31) or the peak loss rates (Fig. 32) indicates good agreement. The principal dependence tested by the correlation is $\tau \propto \tilde{B}_\theta/B_\theta$. The factor of two to five displacement between theory and experiment is not significant since many simplifying assumptions were made (above) in order to make the comparison, and also the calibration uncertainty of the Mirnov signal alone could account for the difference.

Possibly of more significance is the comparison of the peak loss rates with the off-resonance mode "mode particle pumping" loss rates (Fig. 4 of Ref. 3). The data in Fig. 33 indicate that the resonant condition might be broader than predicted in Ref. 3. This is possible since Ref. 3 considered a monoenergetic ion population with a fixed q(r) and a fixed cold plasma $\beta(r)$ profile. It should also be pointed out that we are taking the edge beam ion precession frequency including the finite β correction but not plasma rotation effects.

The inference in Ref. 3 that the frequency changing through the fishbone could mean that the part of velocity space that is lost is also changing so that the resonant condition swept through the beam ions ejecting ions of smaller energy as the frequency slowed down is probably not correct. Since the neutron crosssection changes roughly as $I_n \propto W_B^3$, a strong frequency dependence would be seen in the scaling of $\dot{I}$ (equivalently τ_B) or $\Delta I/I$ and no such dependence was seen.

4.C EMPIRICAL CONFINEMENT MODEL

The number of energetic ions lost from the plasma during the fishbone ($\Delta I/I$) and the instantaneous energetic ion confinement time, τ_B, are both correlated to the neutron oscillation amplitude, $\tilde{I}/I$ (Fig. 10)

$$\tau_B \propto \left(\frac{\tilde{I}}{I}\right)^2 \qquad (23)$$

The neutron fluctuation amplitude is approximately linearly related to the magnitude of the in-out displacement, Δ, of the energetic ions by the internal $n = 1$, $m = 1$ MHD mode (Fig. 12). Thus, (Fig. 16)

$$\tau_B \propto \Delta^{-2} . \qquad (13)$$

The form of Eq. (13) suggests modeling the energetic ion losses by a diffusive process, where the diffusive step length is related to the MHD displacement of the energetic ions on axis, Δ, and the diffusion occurs at the internal fishbone frequency, F. Thus

$$D \simeq \left(\frac{\Delta}{2}\right)^2 F$$

and

$$T_D = \frac{a^2}{D} = \frac{4a^2}{\Delta^2 F} \propto \left(\frac{\tilde{B}_\theta}{B_\theta}\right)^{-1} F^{-1} . \qquad (24)$$

For the single frequency fishbone events, the agreement between this model and experiment can be made quite good over about two orders of magnitude in T_B (Fig. 34) by noting that a threshold of $\tilde{B}\theta/B\theta > 10^{-3}$ was required for observable fishbone losses (Fig. 8). This threshold is equivalent to a threshold of Δ = 1 cm (or about the energetic ion gyroradius). The step size then becomes (Δ-1 cm) yielding

$$T_D = \frac{a^2}{(\Delta-1)^2 F} .$$

Surprisingly, the high frequency events can also be modeled in the same manner, where now the frequency F is about five times higher and the in-out plasma displacement is about 5 cm for the largest high frequency events.

5. CONCLUSIONS

Quantitative measurements of the energetic ion confinement time during fishbone events on PDX were deduced from the beam-target neutron emission. The principal results were:

a) the average confinement $\langle \tau_\beta \rangle$ decreased when βq increased.

b) the instantaneous confinement, τ_β, was inversely related to the MHD perturbation amplitude, $\tilde{B}_\theta / B_\theta$.

c) Energetic ion losses during sawtooth events, and during high frequency events are as large as during 20-kHz fishbone events.

d) The energetic ion losses observed here can be described by the Mode Particle Pumping theory.

ACKNOWLEDGMENTS

The authors thank K. Bol and the PDX Operations group for their support of these experiments. Helpful discussions with P. Beiersdorfer, M. Bell, D. Buchenhauer, L. Chen, R. Goldston, G. Hay, R. Kaita, and R. White are fully appreciated. Technical assistance of G. Estepp and F. Doughty in collecting the data and forming the large data bases was invaluable.

This work supported by U.S. Department of Energy Contract No. DE-AC02-76-CHO-3073.

REFERENCES

[1] D.W. Johnson, M. Bell, M. Bitter, K. Bol, K. Brau, et al., Plasma Physics and Contr. Nucl. Fus. Res. (IAEA, Vienna, 1982) Vol. I, 9.

[2] K. McGuire, R. Goldston, M. Bell, M. Bitter, K. Bol, et al., Phys. Rev. Lett. 50, 891 (1983).

[3] R.B. White, R.J. Goldston, K. McGuire, A. H. Boozer, D.A. Monticello, and W. Park, Phys. Fluids 26, 2958 (1983).

[4] J.D. Strachan, P.L. Colestock, S.L. Davis, D. Eames, P.C. Efthimion, et al., Nucl. Fusion 21, 67 (1981).

[5] G. Zankl, J.D. Strachan, R. Lewis, W. Pettus, and J. Schmotzer, Nucl. Instrum. and Methods 185, 321 (1981).

[6] R.J. Fonck, P. Beiersdorfer, M. Bell, K. Bol, D.A. Boyd, et al., PPPL-2118 (1984). To be published.

[7] G. Hammett and K. McGuire, PPPL-1854 (1982).

[8] R.J. Goldston, D.C. McCune, H.H. Towner, S.L. Davis, R.J. Hawryluk, and G.L. Schmidt, J. Comput. Phys. 43, 61 (1981), description of calculations of beam-beam neutron production appears in R.T. McCann, R.J. Goldston, and D.C. McCune, Bull. Am. Phys. Soc. 27, 971 (1982).

[9] J.D. Strachan and G. Zankel, PPPL-TM-353 (1981).

[10] P. Beiersdorfer, R. Kaita, and R.J. Goldston, Nucl. Fusion 24, 487 (1984).

[11] K.M. McGuire, PPPL-2134 (1984).

[12] Princeton Plasma Physics Laboratory Annual Report, PPPL-Q-38, 1980.

FIGURE CAPTIONS

1) Time evolution of a) the 2.5-MeV neutron emission and b) the Mirnov signal through a fishbone instability having only a nominally 20-kHz oscillation. The values of the quantities I(t), I(t), and $I(t_0)$ needed to calculate the instantaneous confinement time, τ_B [Eq. (3)] are indicated.

2) The neutron emission from PDX $D^0 \rightarrow D^+$ beam heated plasmas scaled against the expected classical dependence ($n_e^{1/2} T_e^{3/2} P_B W_B^2$). The beam power, P_B, is that incident upon the plasma and is greater than that absorbed by the plasma. n_e is the volume-averaged density, T_e is the central electron temperature, and W_B is the beam voltage.

3) The neutron emission, I_n, from PDX $D^0 \rightarrow D^+$ beam heated plasmas scaled against T_e at constant beam voltage and beam power. The dependence $T_e^{3/2}$ is expected from classical electron drag. The solid line is a least squares fit to the data.

4) The neutron emission normalized to the electron temperature and beam power, $I_n/T_e^{3/2}P_B$, scaled with a) the volume-averaged electron density, $\langle n_e \rangle$, and b) the neutral mean-free path for a beam neutral ℓ/a. The data are restricted to constant beam voltage, (42.5 keV < W_B < 46 kV).

5) The experimental neutron emission compared to the TRANSP calculation of the beam-target plus beam-beam neutron emissions. The calculations use the experimental electron temperature and electron density profiles to calculate the classical deposition and slowing down of the beam ions. The solid points are for Co perpendicular beam injection and the open points are for counter perpendicular beam (obtained by reversing the plasma current).

6) Time evolution of a) the fishbone frequency, F, b) the magnetic oscillation amplitude, $\tilde{B}_\theta/B_\theta$, and c) the deduced instantaneous energetic ion confinement time, τ_B, for the fishbone in Fig. 1.

7) Scaling of the energetic ion confinement time, τ_B, with the magnetic oscillation amplitude, $\tilde{B}_{\theta/B_\theta}$ through the time evolving fishbone event shown in Figs. 1 and 6.

8) The peak magnetic perturbation amplitude, $\tilde{B}\theta/B\theta$, and the fishbone frequency, F, at the peak amplitude for the events which make up the data base of 20-kHz fishbones. The open points had a measureable neutron drop ($\Delta I/I > 0.2\%$) while the solid points had $\Delta I \approx 0$. Evidently, a threshhold in magnetic perturbation amplitude, of about $\tilde{B}_\theta/B\theta > 10^{-3}$, is required for a measureable energetic ion loss at a fishbone.

9) The minimum energetic ion confinement time, τ_B, as a function of the peak magnetic perturbation amplitude $\tilde{B}\theta_{/B\theta}$ for the single frequency fishbone events.

10) The fraction of energetic ions lost in the fishbone ($\Delta I_n/I_n$) as a function of the amplitude of the neutron oscillation, at the fishbone frequency, $\tilde{I}_n/I_n$, for the single frequency fishbone events. The line is a least squares fit to the data.

11) The best fit for the change in fishbone frequency (ΔF) (from before the neutrons began to decay until after they had finished decaying) shows a dependence of about $F_i^{\,2}(\tilde{B}\theta/B\theta)^{1/4}$ with a correlation coefficient of $R^2 = 0.70$. F_i is the initial frequency.

12) Calculated neutron fluctuation amplitude, $\tilde{I}_n/I_n$, to an in-out movement, Δ, of the neutron emitting plasma. The points are calculated and the line is a fit to the points.

13) Phase correlation of a) the movement of the plasma center as determined by the central soft X-rays and b) the neutron fluctuations at the fishbone frequency. The neutron signal peaks when the plasma center has its maximum displacement towards the neutron detector. The soft X-ray measurement is actually an up-down measurement, however in this figure the phase has been changed to represent the in (negative) and out (positive) movement of the plasma in front of the neutron detector.

14) Toroidal phase information for two neutron detectors spaced 180° toroidally around PDX.

15) a) Poloidal phase information from two neutron detectors at the same toroidal location but displaced poloidally by 54°.

b) The calculated detector response to a decaying neutron signal superimposed on an m = 1 displacement of the neutron emitting region of the plasma (rotating in the ion diamagnetic direction). The similarity in amplitude and phase of the modeled response (b) with the data (a) indicates that the neutron fluctuations are caused by displacement of the reacting plasma.

16) The relation between the energetic ion confinement, τ_B, and the magnitude of the in-out plasma motion, Δ, which was determined from the neutron fluctuation amplitude, $\tilde{I}_n/I_n$ (Fig. 12). The open points are the single frequency fishbone events and the solid points are double frequency fishbones with a large low frequency perturbation.

17) The time evolution of a) the neutron emission and b) the Mirnov signal for a high frequency event.

18) Time evolution of a) the MHD oscillation frequency, FH, b) the MHD magnetic perturbation amplitude, $\tilde{B}\theta/B\theta$, and c) the energetic ion confinement time, τ_B, through the high frequency event in Fig. 17.

19) Time evolution of a) the neutron emission, I_n, and b) the Mirnov signal for a double frequency fishbone.

20) Time evolution of a) the two frequencies, b) the lower frequency magnetic perturbation amplitude, c) the higher frequency magnetic perturbation amplitude, d) the experimental energetic ion confinement time, τ_B, e) the empirical confinement time, τ_L, from the single frequency fishbones (Sec. 3.B.1), and f) the empirical confinement time, τ_H, from the high frequency events (Sec. 3.B.2) through the double frequency fishbone in Fig. 19. The double frequency event is essentially the linear combination of the high and low frequency events within the uncertainties of our ability to describe empirically the high frequency event.

21) The minimum energetic ion confinement time, τ_B, for double frequency fishbones as a linear combination of the sum of the empirically deduced high and low frequency events, τ_H and τ_L, using the measured magnetic perturbations at the time of the minimum energetic ion confinement. The solid point is the case without a low frequency (Fig. 18), the open points are ones where the lower frequency losses dominate, and the "Δ" points are ones where the higher frequency losses dominate.

22) Time evolution of a) the neutron emission, I_n, b) the central soft X-rays, and c) the Mirnov signal for a PDX sawtooth event of the type with large energetic ion losses.

23) The energetic ion confinement time, τ_B, as a function of the external magnetic perturbation amplitude $\tilde{B}\theta/B\theta$ for the sawtooth events (e.g., Fig. 22). The shaded region is the range of the data for the single frequency fishbones (Fig. 9).

24) Location of the plasmas having the various types of fishbone events in βq space. a) The single frequency, "classic" fishbone, b) the plasmas which form the $\langle \tau_B \rangle$ data base, c) the double frequency events where the open points are dominated by the lower frequency and the solid points are dominated by the higher frequency, and d) the sawtooth events.

25) Scaling of the average energetic ion confinement, $\langle \tau_B \rangle$, with βq. The PLT sawtooth region is indicative of the calculated $\langle \tau_B \rangle$ for sawtooth events which probably feature only an internal energetic ion redistribution and not any energetic ion losses from the plasma [4]. The PLT a = 28 cm point indicates a possible PLT fishbone event [12]; β was estimated from plasma temperatures (and thus is highly uncertain). τ_s is a typical PDX slowing down duration and τ_n is the cross-section weighted beam slowing down time for typical PDX conditions. $\langle \tau_B \rangle$ is measured in msec.

26) Scaling of the average energetic ion confinement time, $\langle \tau_B \rangle$, for the data in Fig. 25 when a) q is varied but β is held constant ($0.8 < \beta < 1.2$) or b) β is varied but q is held constant ($2 < q < 2.5$).

27) Scaling of the average energetic ion confinement time, $\langle \tau_B \rangle$, with the parameter $B_\phi^3/\beta q^2$, which was obtained from a regression analysis using the data in Fig. 25.

28) Dependence of the average energetic ion confinement time, $\langle \tau_B \rangle$, with the toroidal magnetic field at constant βq ($0.03 < \beta q < 0.04$).

29) The ratio of the two frequencies, FH/F, in the double frequency fishbones as a function of βq. The open points have the energetic ion losses dominated by the higher frequency, the solid points have the energetic ion losses dominated by the lower frequency.

30) Comparison of the density dependence of (a) the neutron emission (normalized to the input power) and (b) the expected fraction, ξ, of full energy beam ions trapped inside a/2 for PLT and PDX.

31) Time evolution of the theoretical minimum confinement time, τ_{min} predicted by the mode particle pumping theory (solid points) for the fishbone event in Fig. 1 (open points).

32) Comparison of the experimental energetic ion confinement time, τ_B, with the minimum confinement time, τ_{min}, predicted by the Mode Particle Pumping theory.

33) The percentage of beam ions lost for single frequency fishbone events with ($0.6\% < \tilde{B}\theta/B\theta < 1\%$) as a function of the fishbone frequency normalized to the ion cyclotron frequency [3]. The line is the prediction of the Mode Particle Pumping theory for $\tilde{B}\theta/B\theta = 1\%$ (as measured at the Mirnov coil).

34) The energetic ion confinement time, τ_B, compared to the simple diffusive loss model, τ_D. The solid points are single frequency events and the open circles are double frequency events.

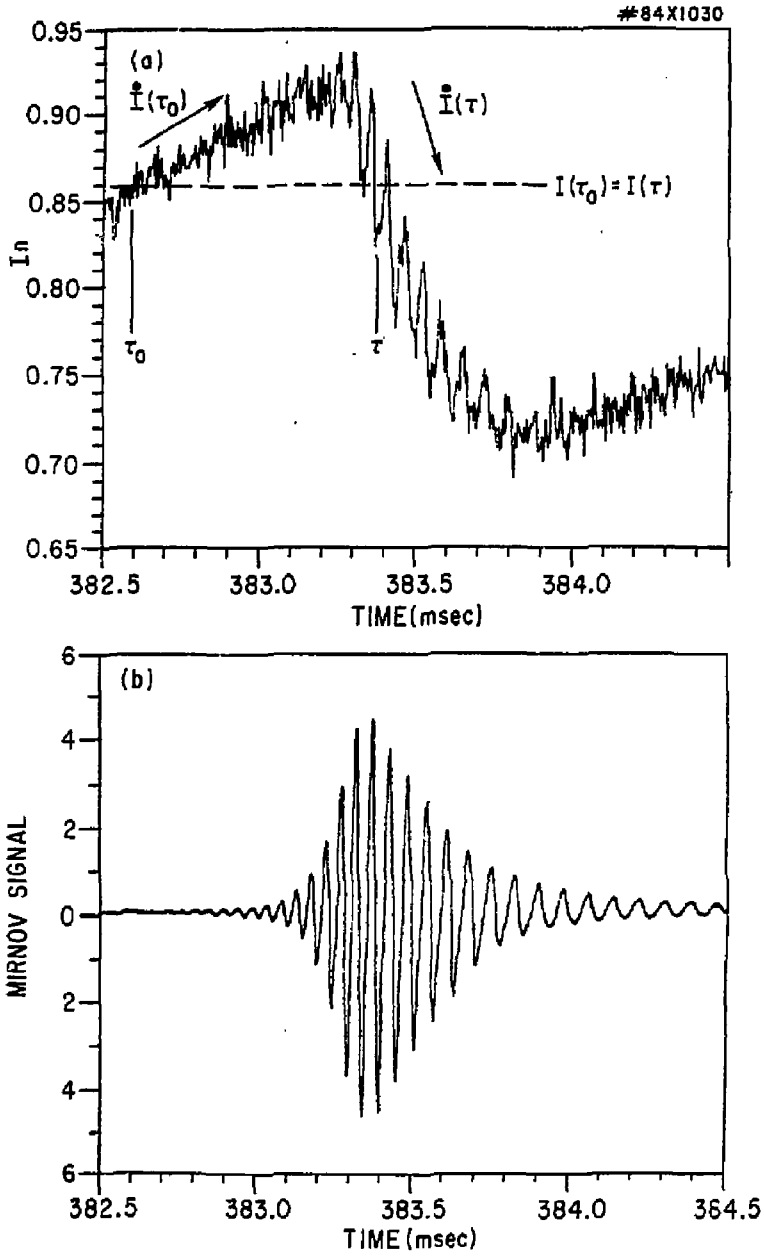
#84X1030
(a)
$\dot{I}(\tau_0)$
$\dot{I}(\tau)$
$I(\tau_0) = I(\tau)$
τ_0
τ
In
0.95
0.90
0.85
0.80
0.75
0.70
0.65
382.5
383.0
383.5
384.0
TIME(msec)
(b)
MIRNOV SIGNAL
6
4
2
0
2
4
6
382.5
383.0
383.5
384.0
384.5
TIME (msec)

Fig. 1

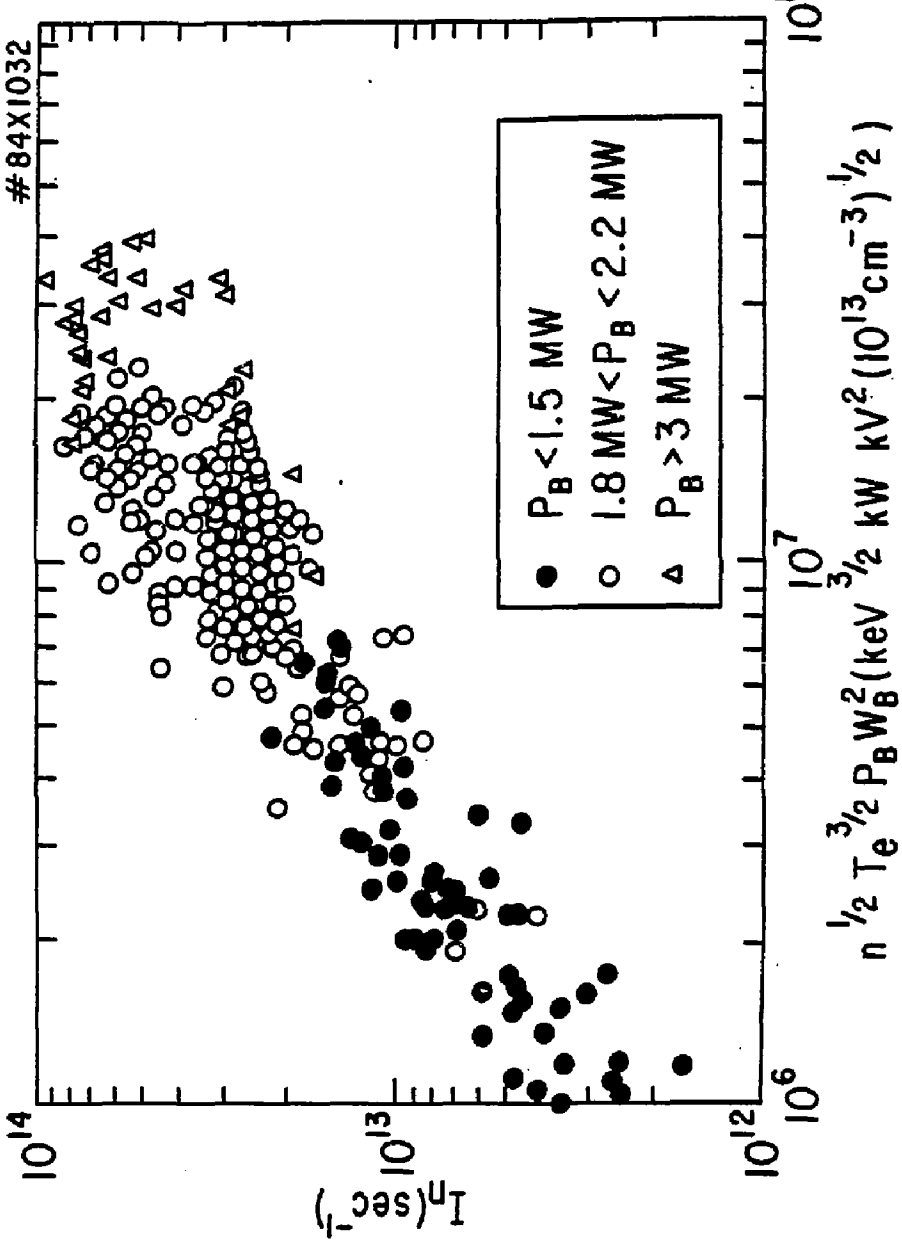
#84X1032
$I_n(sec^{-1})$
10^{14}
10^{13}
10^{12}
10^{6}
10^{7}
10^{8}
$n^{1/2}\ T_e^{3/2}\ P_B W_B^2 (keV^{3/2}\ kW\ kV^2 (10^{13} cm^{-3})^{1/2})$
$P_B < 1.5$ MW
1.8 MW $< P_B <$ 2.2 MW
$P_B > 3$ MW

Fig. 2

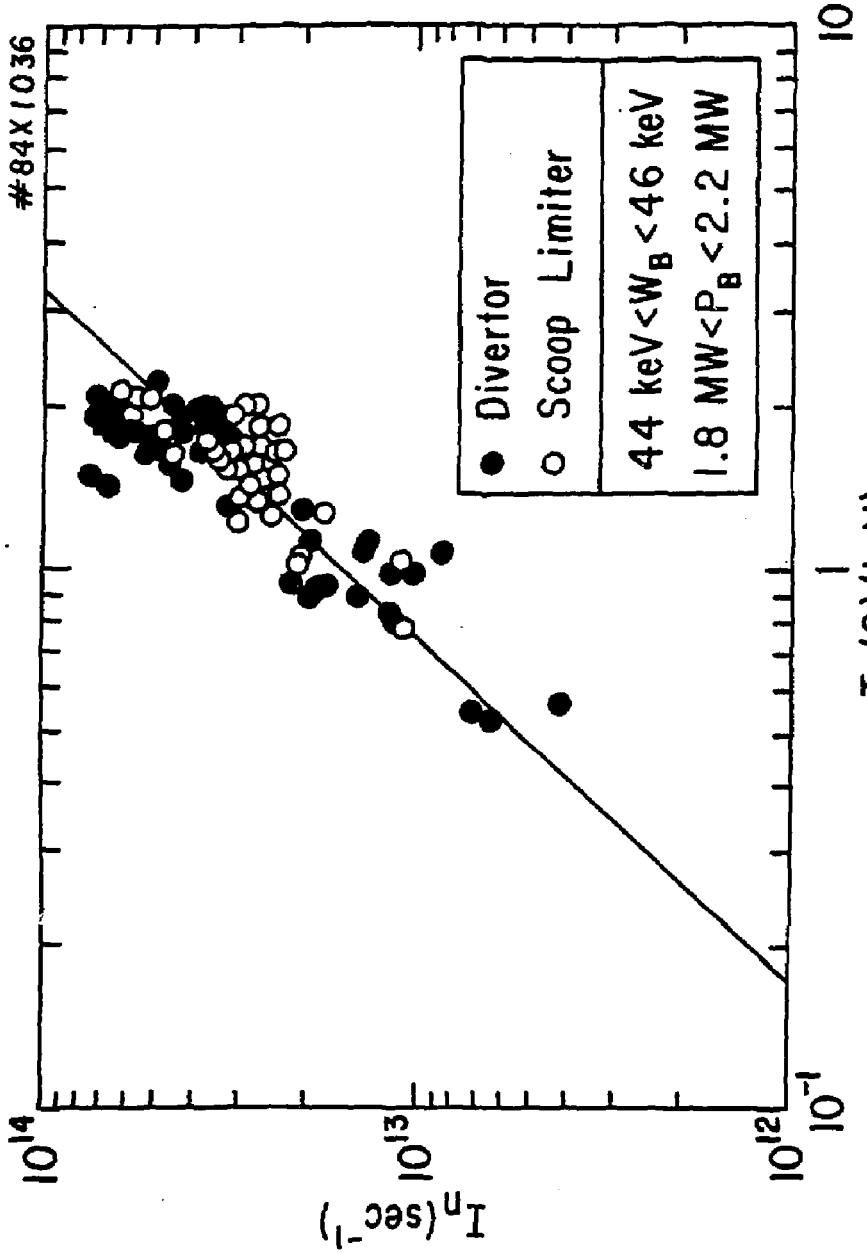
#84X1036
$I_n(sec^{-1})$
10^{14}
10^{13}
10^{12}
10^{-1}
1
10
$T_e(0)(keV)$
Divertor
Scoop Limiter
44 keV<W_B<46 keV
1.8 MW<P_B<2.2 MW

Fig. 3

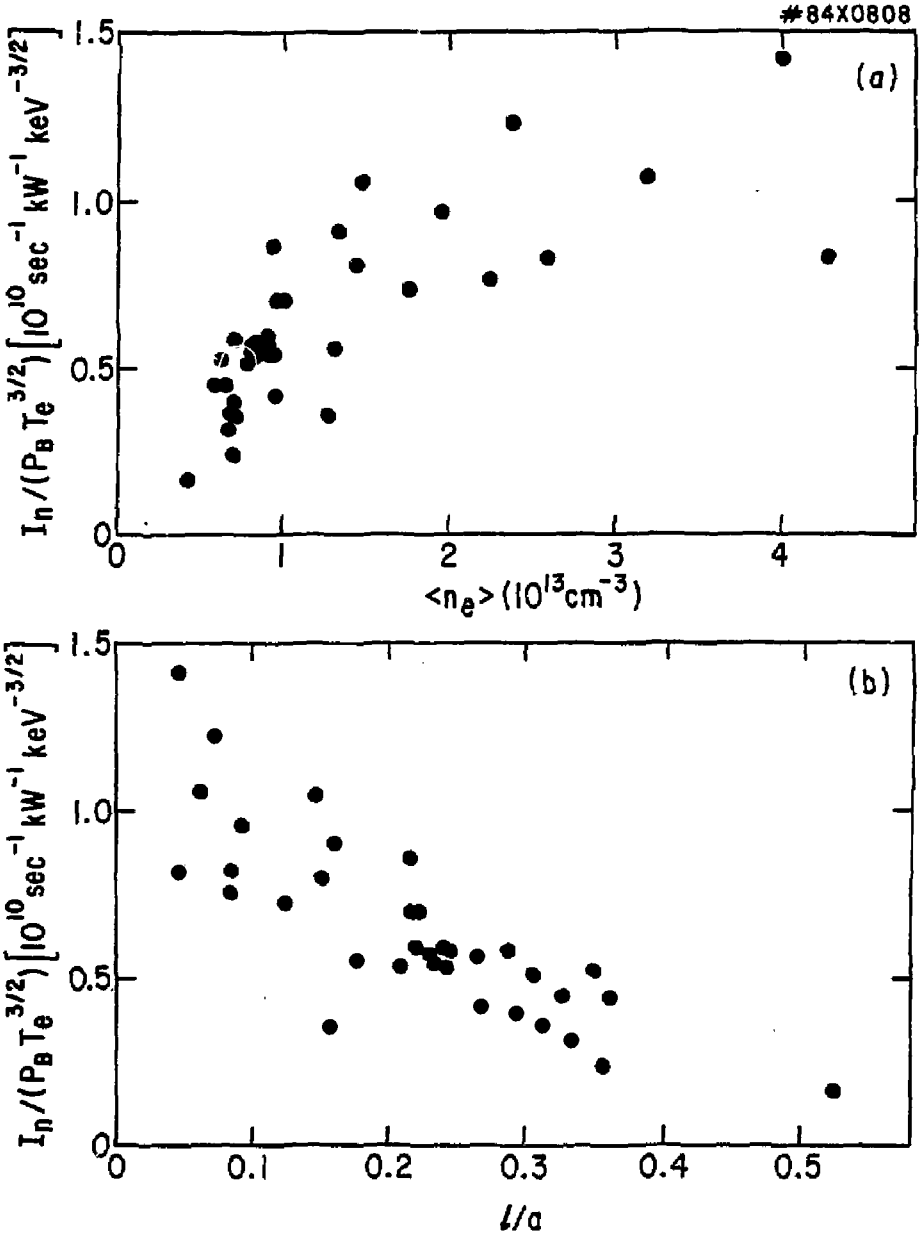
#84X0808
(a)
$I_n/(P_B T_e^{3/2})$ [10^{10} sec^{-1} kW^{-1} $keV^{-3/2}$]
1.5
1.0
0.5
0
0
1
2
3
4
$\langle n_e \rangle$ (10^{13} cm^{-3})
(b)
$I_n/(P_B T_e^{3/2})$ [10^{10} sec^{-1} kW^{-1} $keV^{-3/2}$]
1.5
1.0
0.5
0
0
0.1
0.2
0.3
0.4
0.5
l/a

Fig. 4

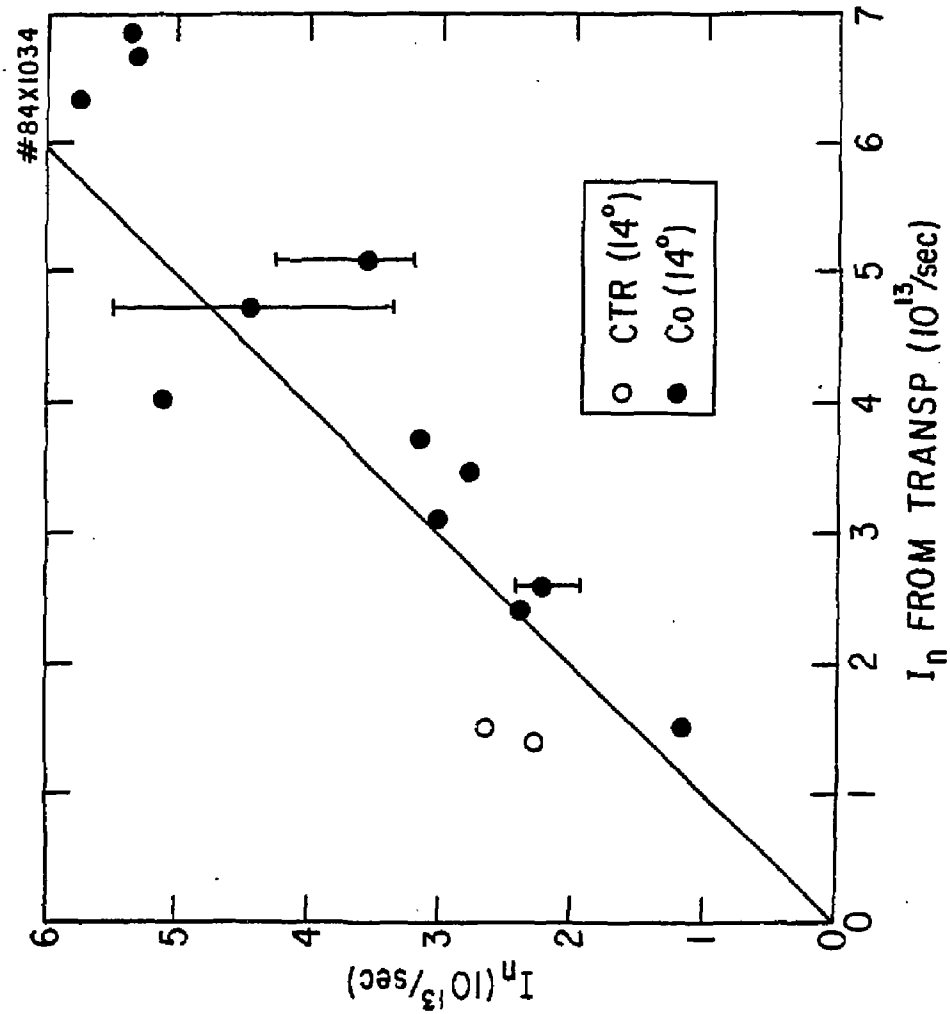

Fig. 5

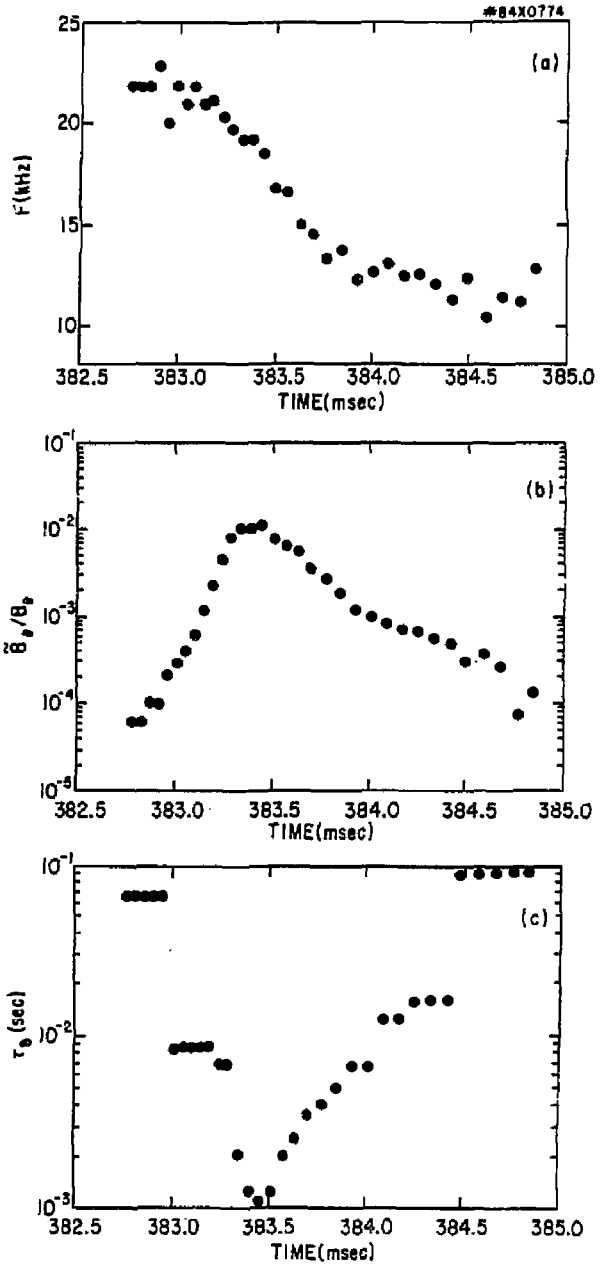
#84X0774
(a)
F(kHz)
25
20
15
10
382.5
383.0
383.5
384.0
384.5
385.0
TIME(msec)
(b)
$\tilde{B}_\theta/B_\theta$
10^{-1}
10^{-2}
10^{-3}
10^{-4}
10^{-5}
TIME(msec)
(c)
τ_θ (sec)
10^{-1}
10^{-2}
10^{-3}
TIME(msec)

Fig. 6

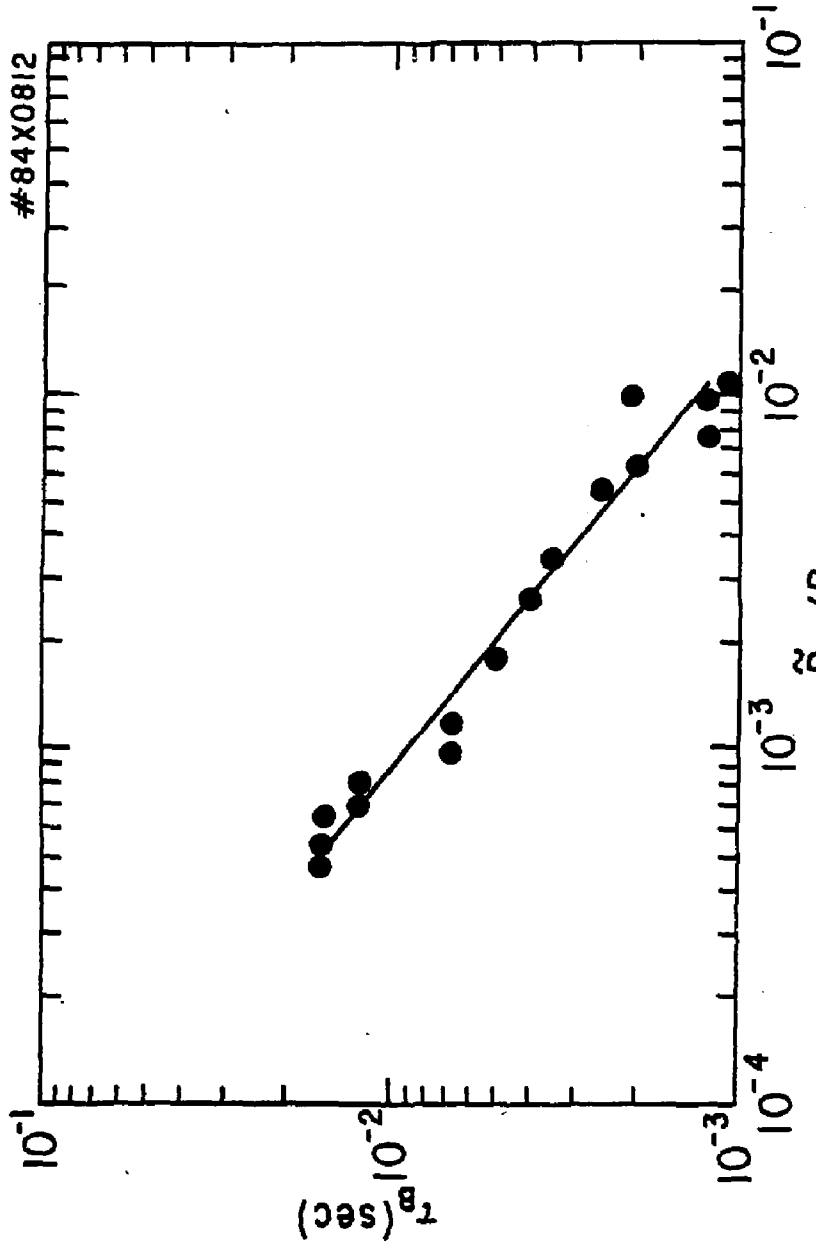

Fig. 7

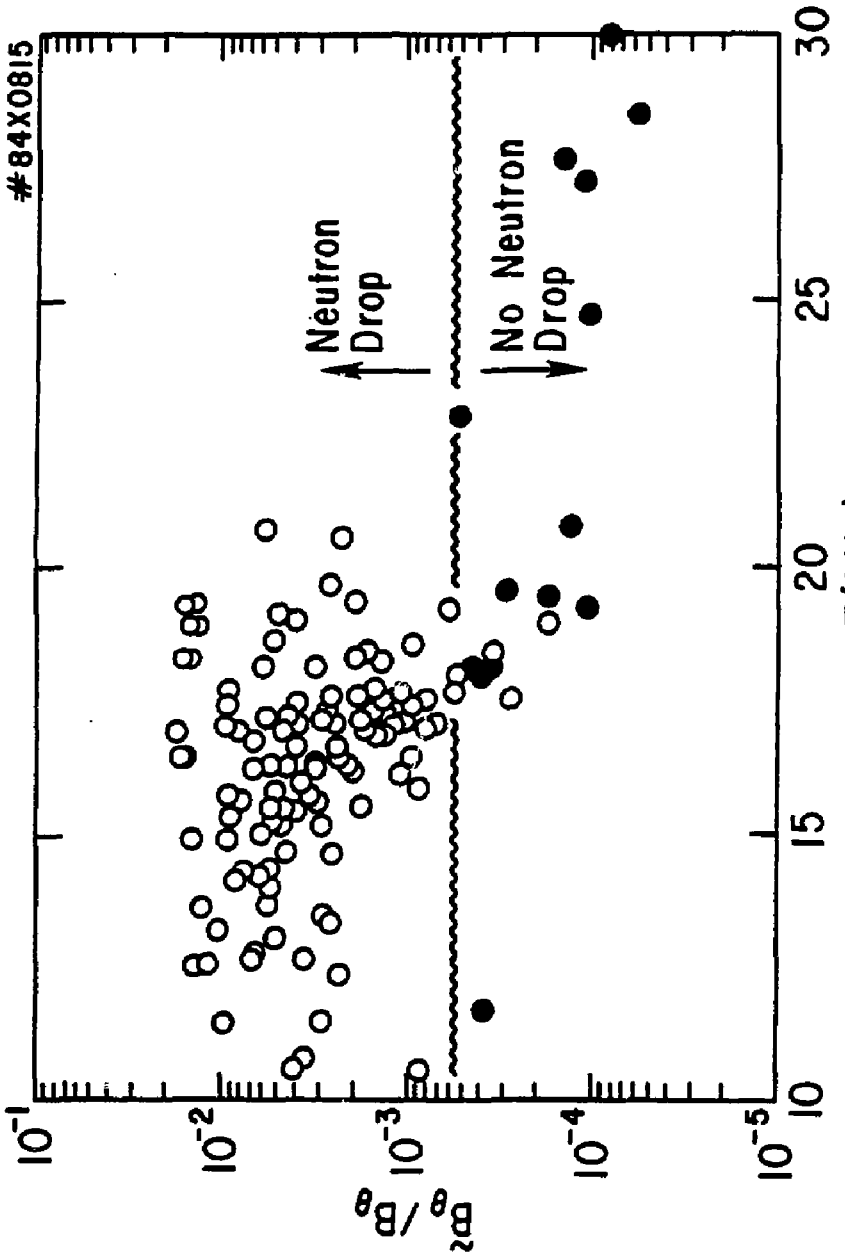
#84X0815
Neutron Drop
No Neutron Drop
B_θ^2/B_θ
F(kHz)
10^{-1}
10^{-2}
10^{-3}
10^{-4}
10^{-5}
10
15
20
25
30

Fig. 8

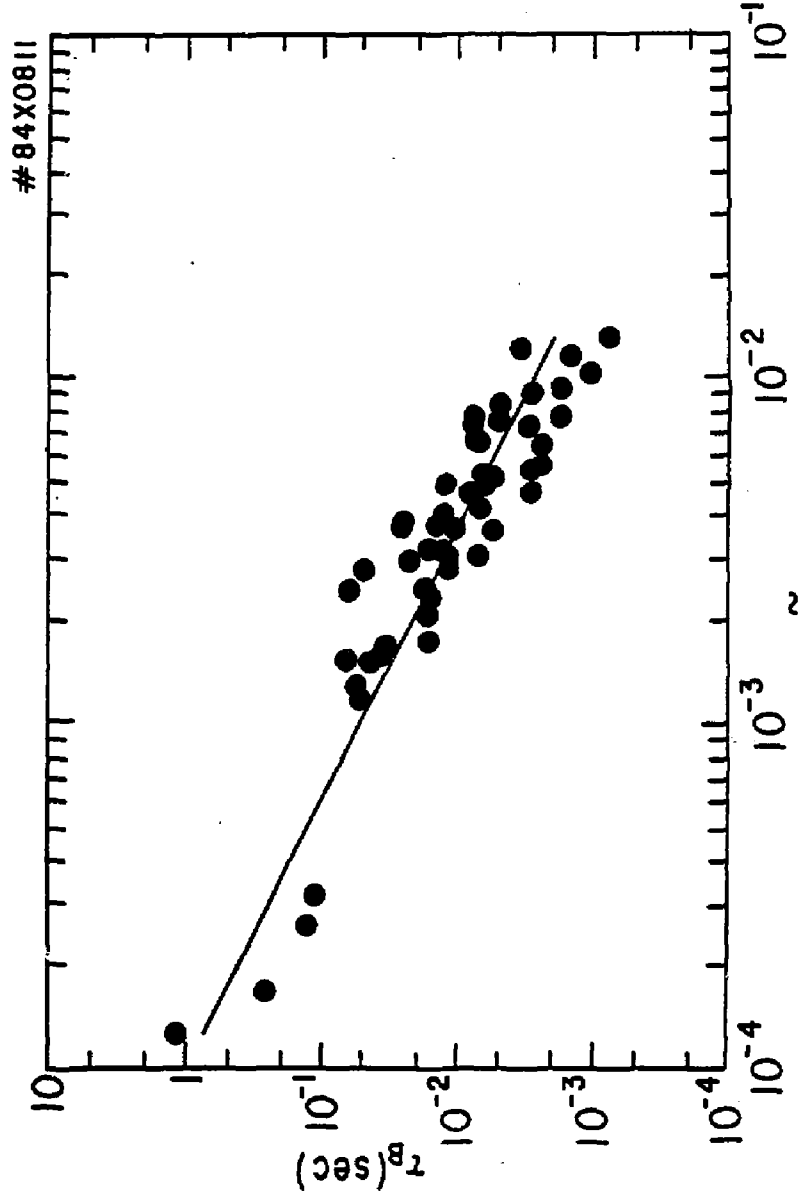

Fig. 9

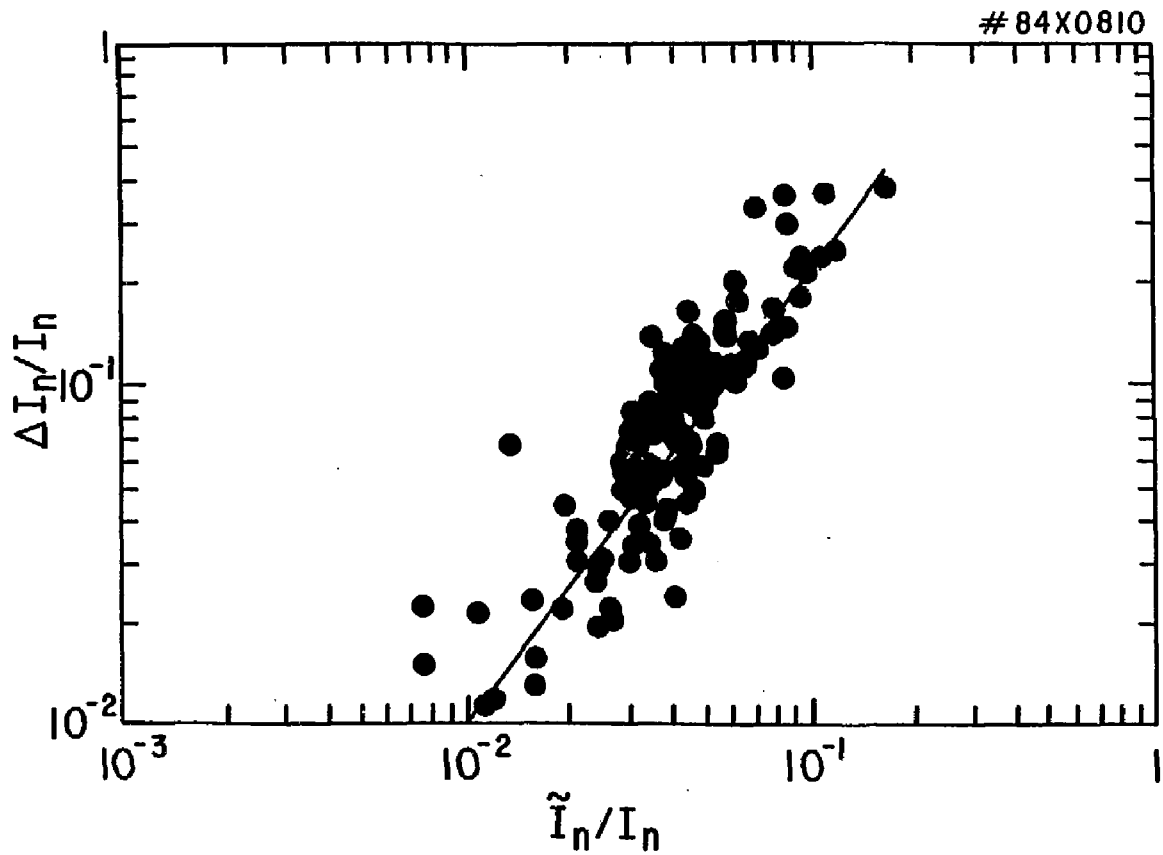

Fig. 10

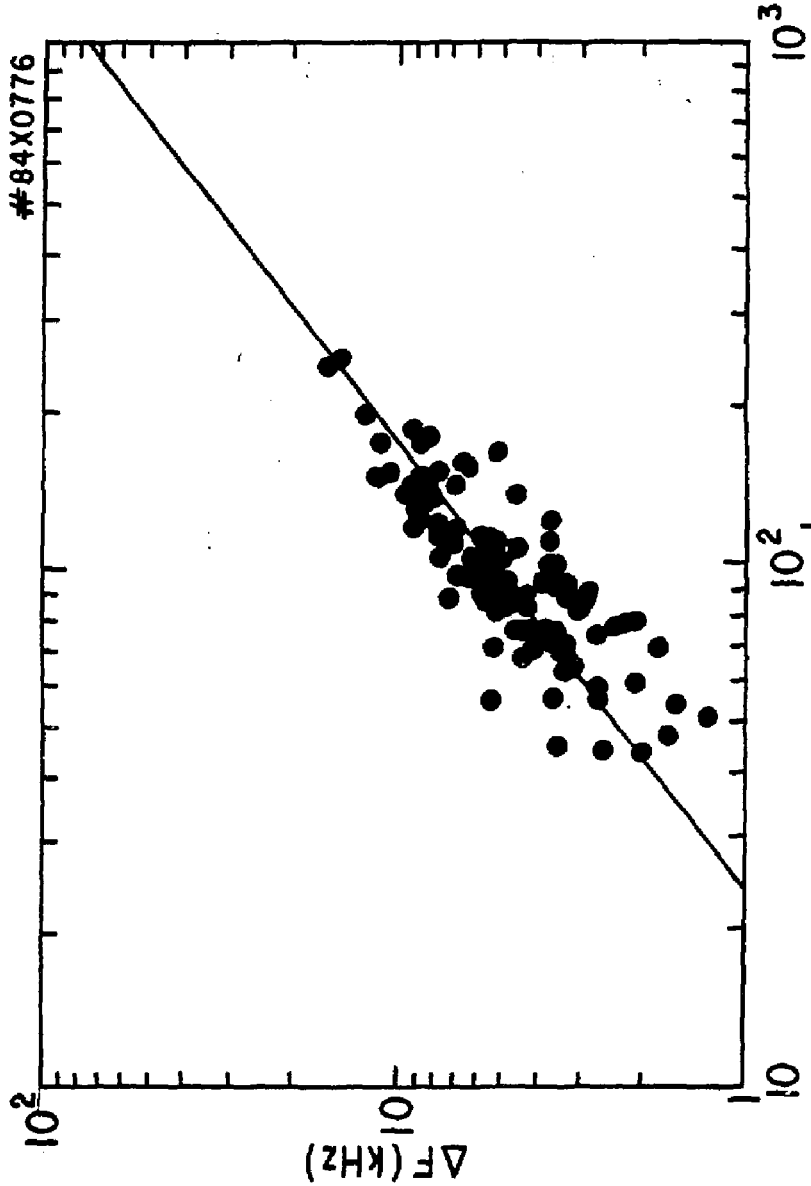
#84X0776
10^2
10^3
ΔF (kHz)
$F_i^2 \left(\frac{\tilde{B}_\theta}{B_\theta}\right)^{1/4}$

Fig. 11

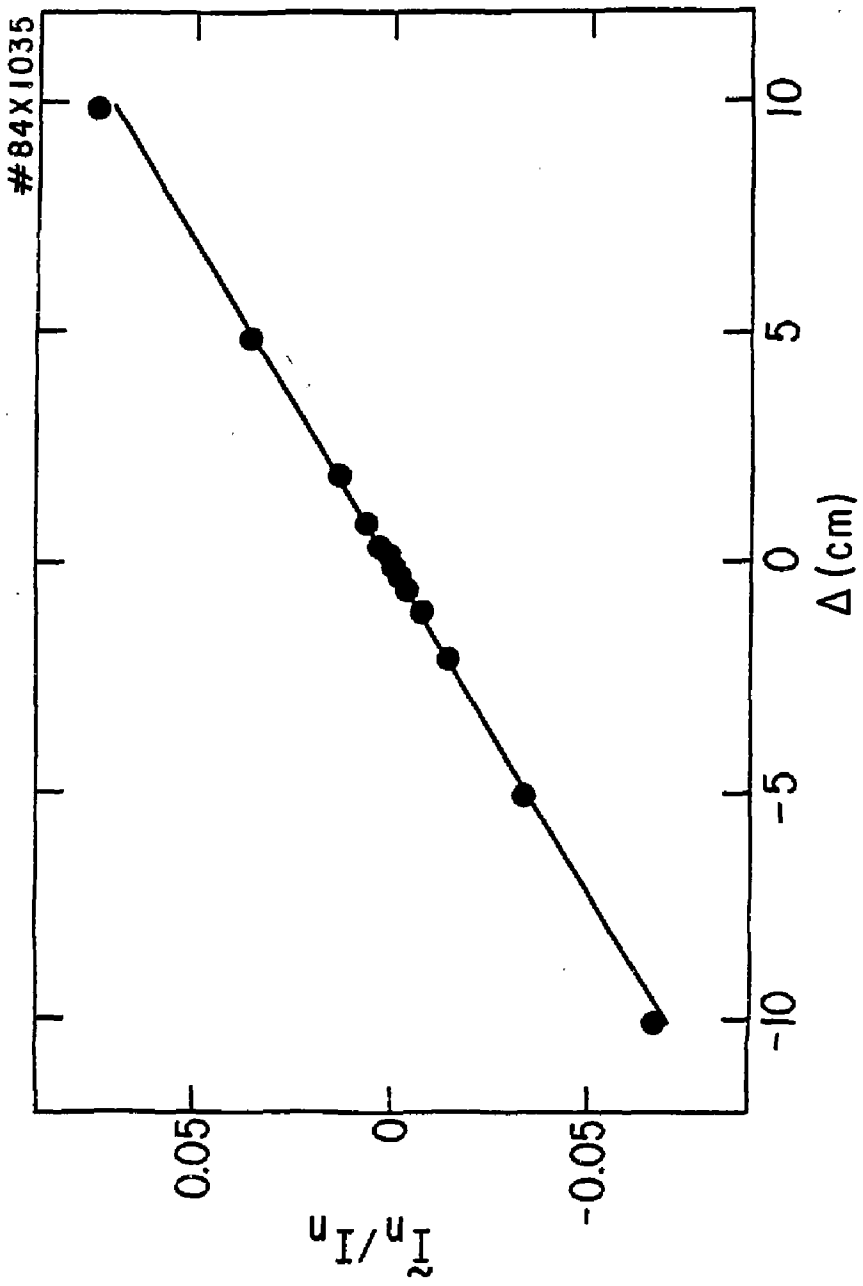

Fig. 12

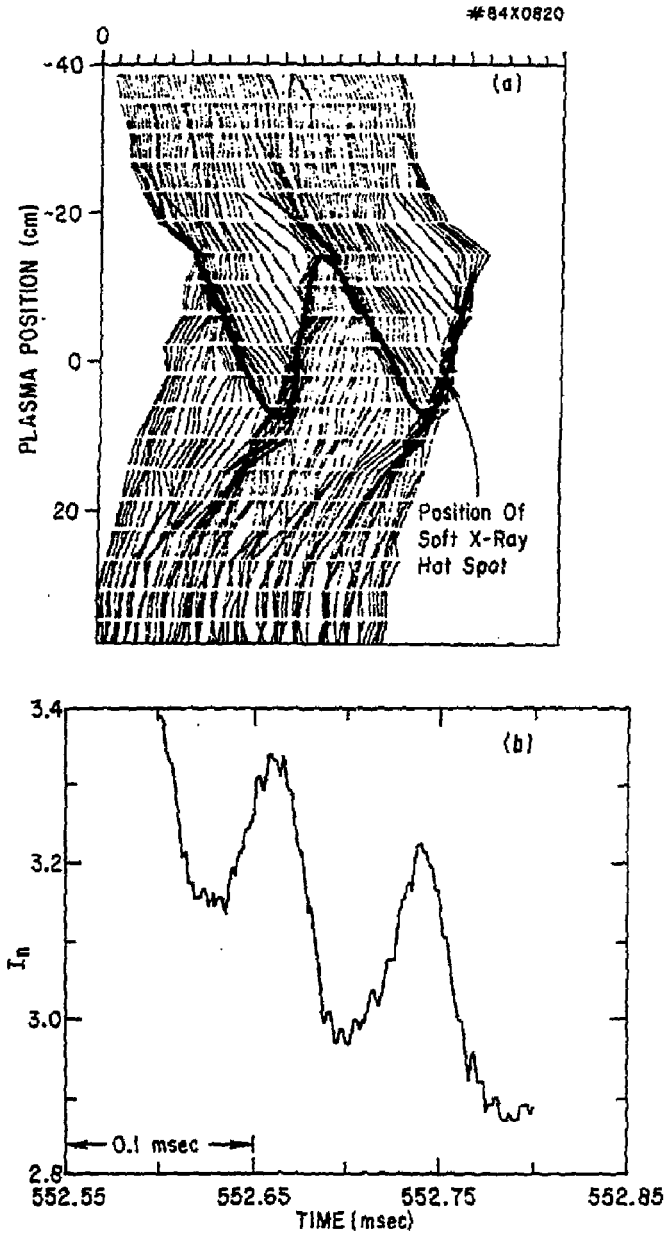
#84X0820
(a)
PLASMA POSITION (cm)
0
-40
-20
0
20
Position Of
Soft X-Ray
Hot Spot
(b)
I_n
3.4
3.2
3.0
2.8
0.1 msec
552.55
552.65
552.75
552.85
TIME (msec)

Fig. 13

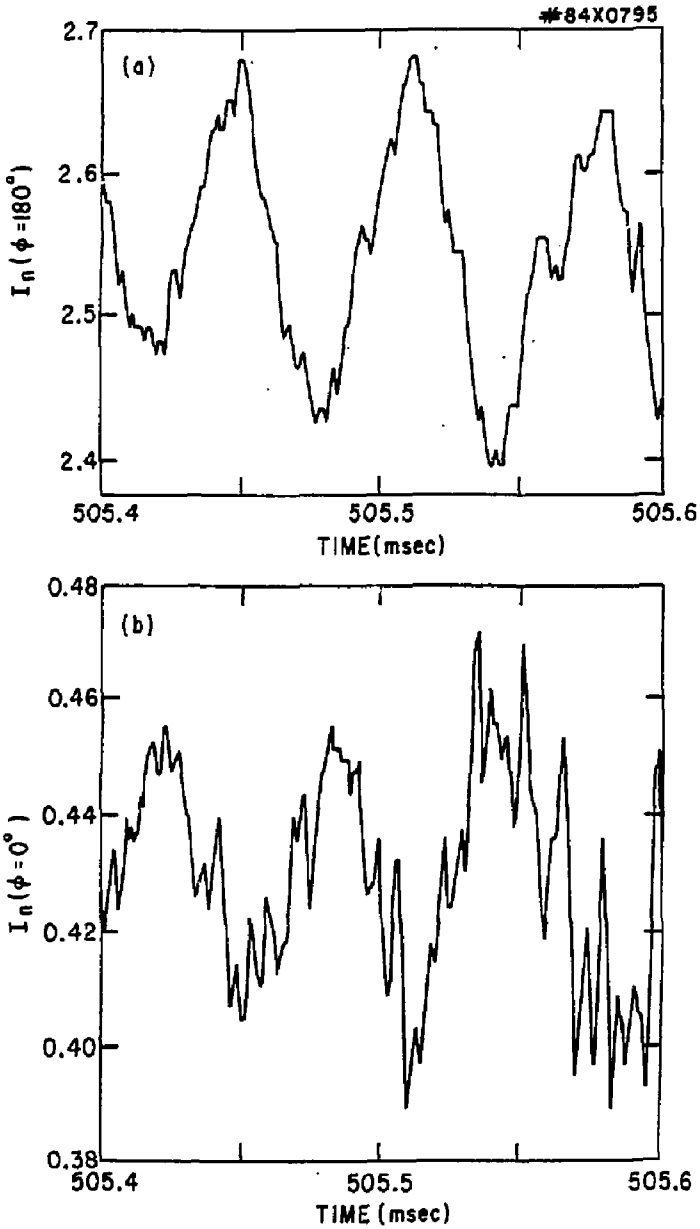
#84X0795
(a)
2.7
2.6
2.5
2.4
$I_n(\phi=180°)$
505.4
505.5
505.6
TIME(msec)
(b)
0.48
0.46
0.44
0.42
0.40
0.38
$I_n(\phi=0°)$
505.4
505.5
505.6
TIME (msec)

Fig. 14

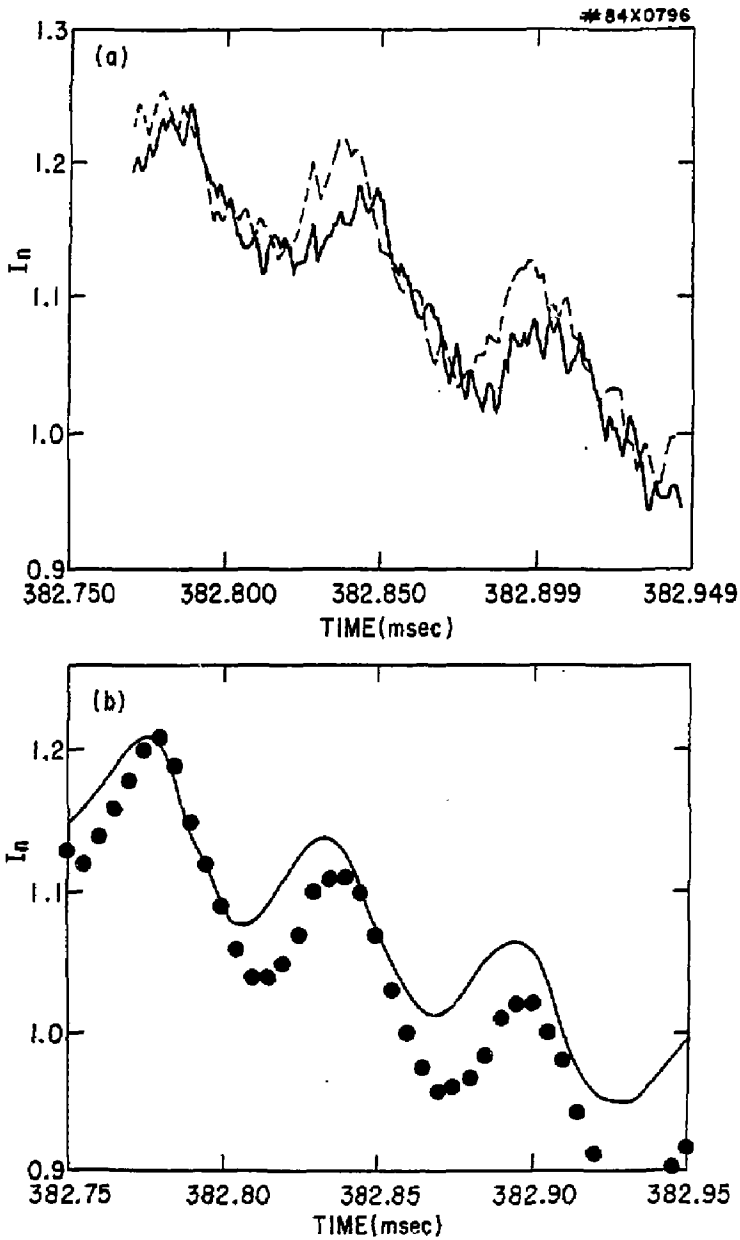
#84X0796
(a)
1.3
1.2
1.1
1.0
0.9
I_n
382.750
382.800
382.850
382.899
382.949
TIME(msec)
(b)
1.2
1.1
1.0
0.9
I_n
382.75
382.80
382.85
382.90
382.95
TIME(msec)

Fig. 15

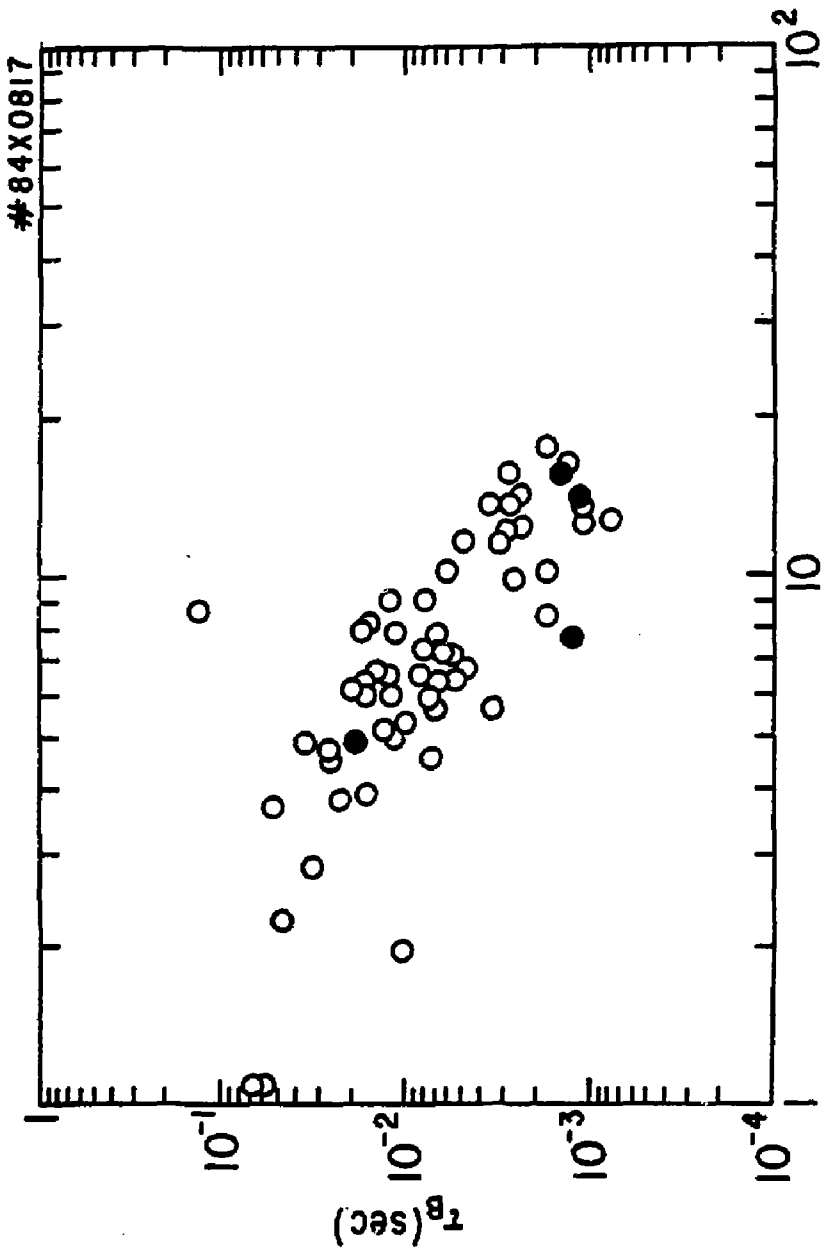

Fig. 16

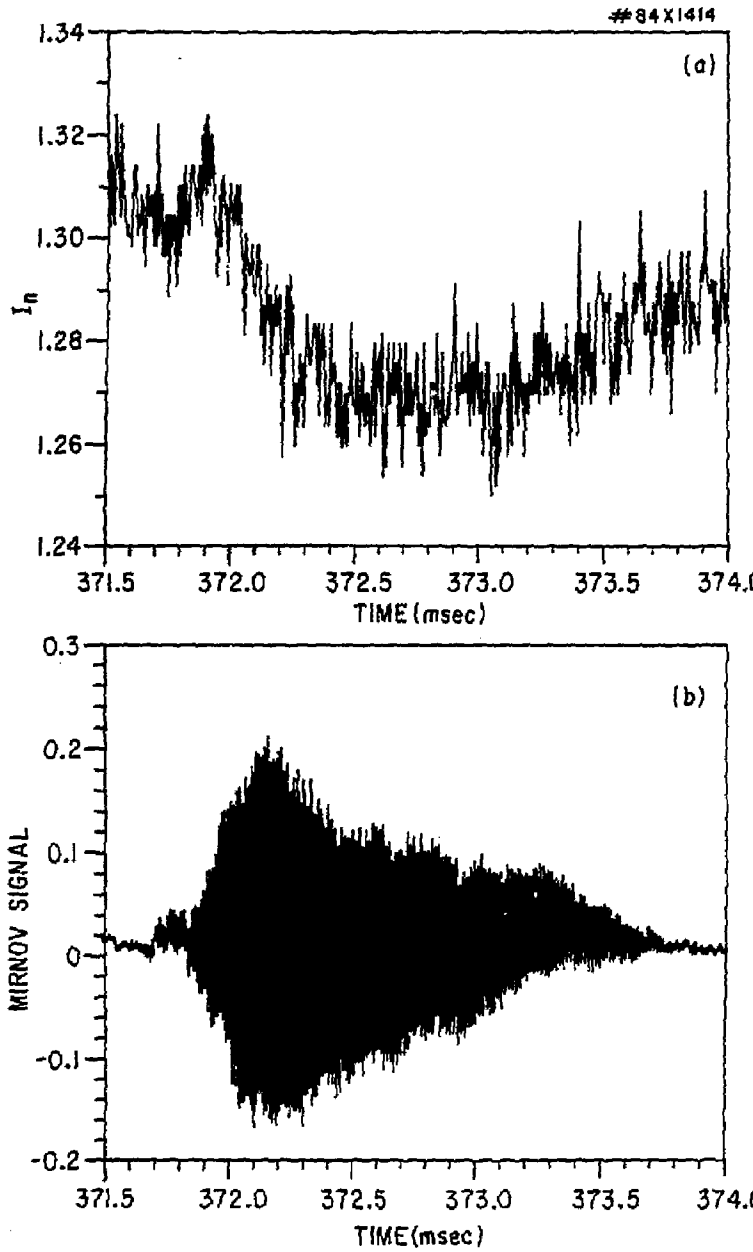
#84X1414
(a)
1.34
1.32
1.30
1.28
1.26
1.24
I_n
371.5
372.0
372.5
373.0
373.5
374.0
TIME (msec)
(b)
0.3
0.2
0.1
0
-0.1
-0.2
MIRNOV SIGNAL
371.5
372.0
372.5
373.0
373.5
374.0
TIME(msec)

Fig. 17

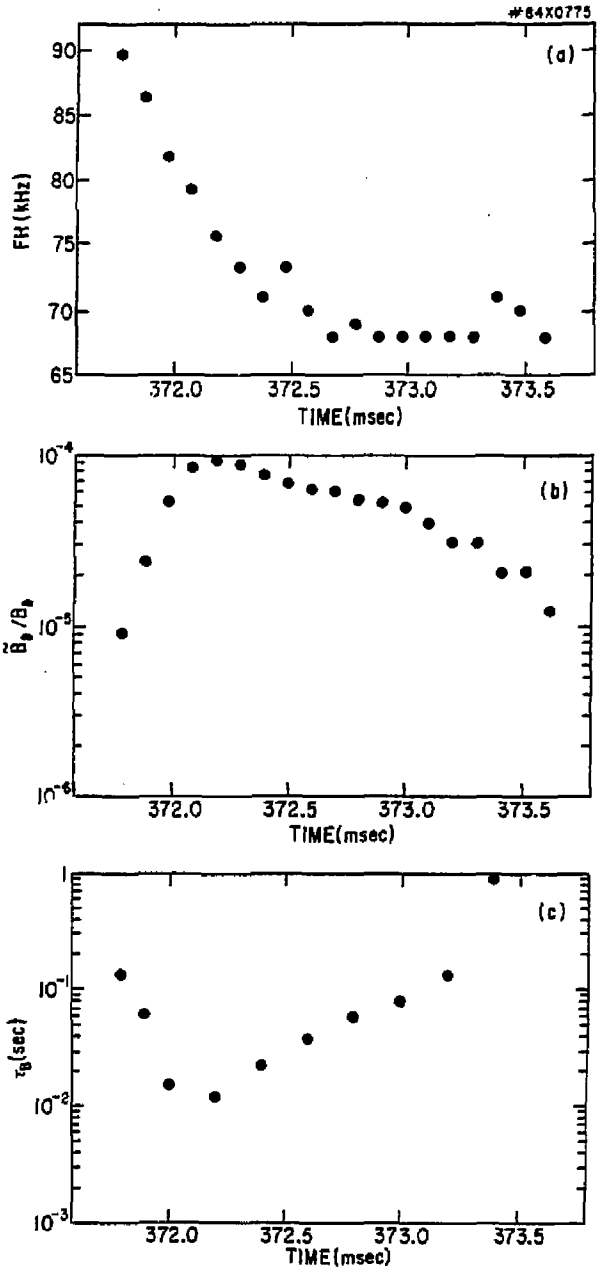
#64X0775
(a)
FH(kHz)
90
85
80
75
70
65
372.0
372.5
373.0
373.5
TIME(msec)
(b)
$\tilde{B}_\theta/B_\phi$
10^{-4}
10^{-5}
10^{-6}
372.0
372.5
373.0
373.5
TIME(msec)
(c)
τ_B(sec)
10^{-1}
10^{-2}
10^{-3}
372.0
372.5
373.0
373.5
TIME(msec)

Fig. 18

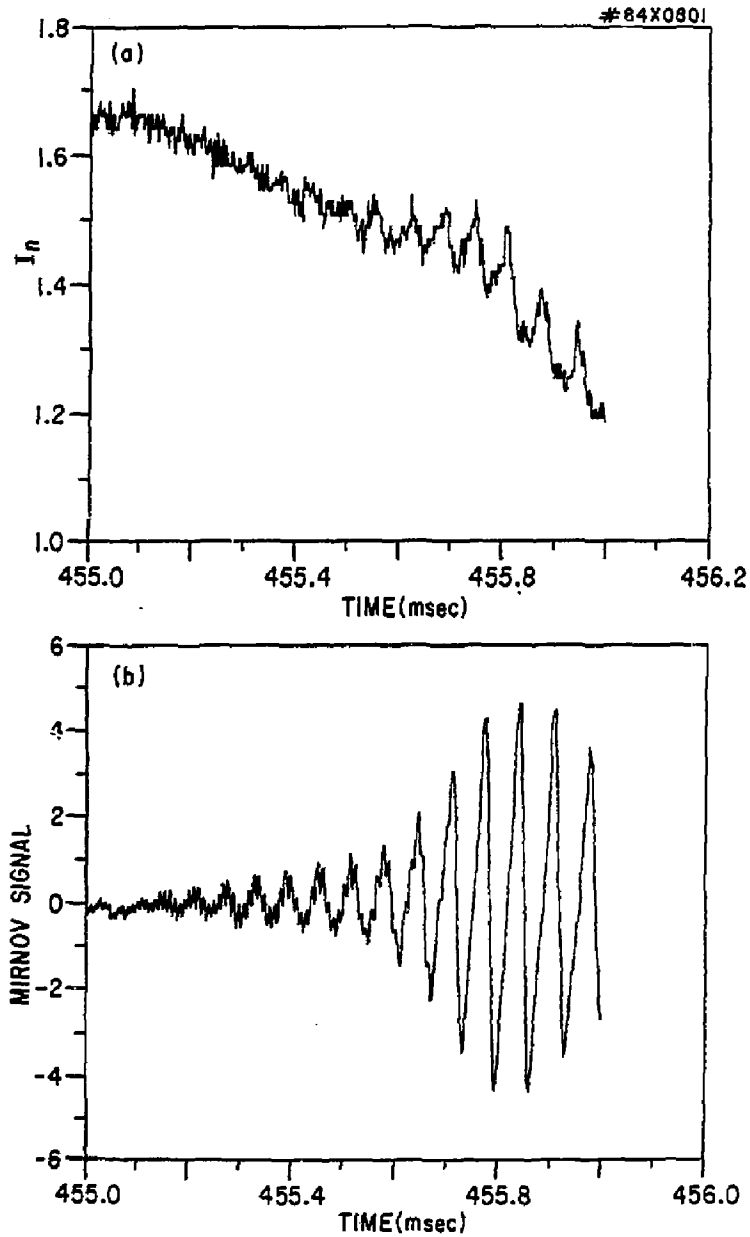
#84X0801
(a)
1.8
1.6
1.4
1.2
1.0
I_n
455.0
455.4
455.8
456.2
TIME(msec)
(b)
6
4
2
0
-2
-4
-6
MIRNOV SIGNAL
455.0
455.4
455.8
456.0
TIME(msec)

Fig. 19

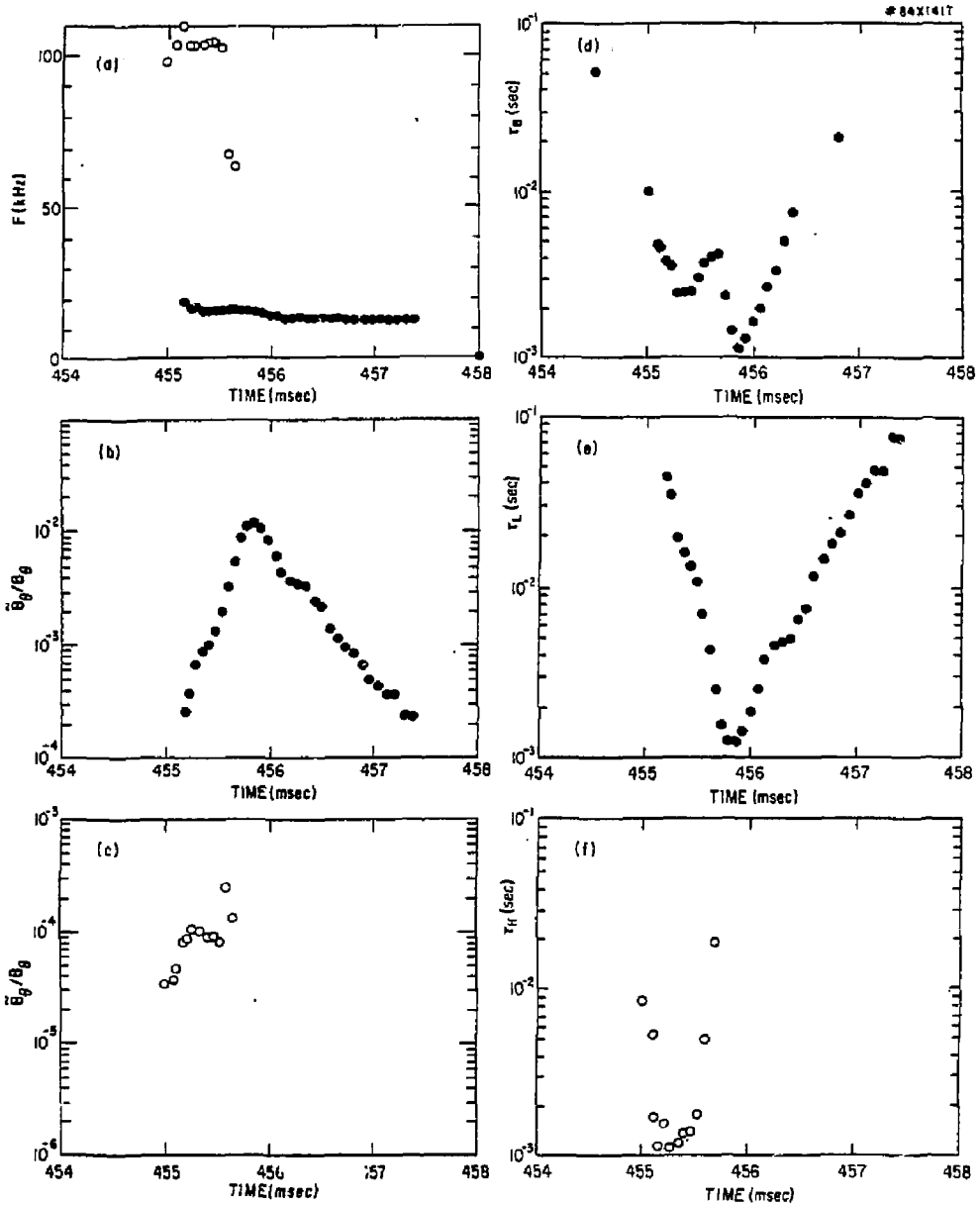
(a)
F(kHz)
TIME(msec)
(b)
$\tilde{B}_\theta/B_\theta$
TIME(msec)
(c)
$\tilde{B}_\theta/B_\theta$
TIME(msec)
(d)
τ_B (sec)
TIME (msec)
(e)
τ_L (sec)
TIME (msec)
(f)
τ_H (sec)
TIME (msec)

Fig. 20

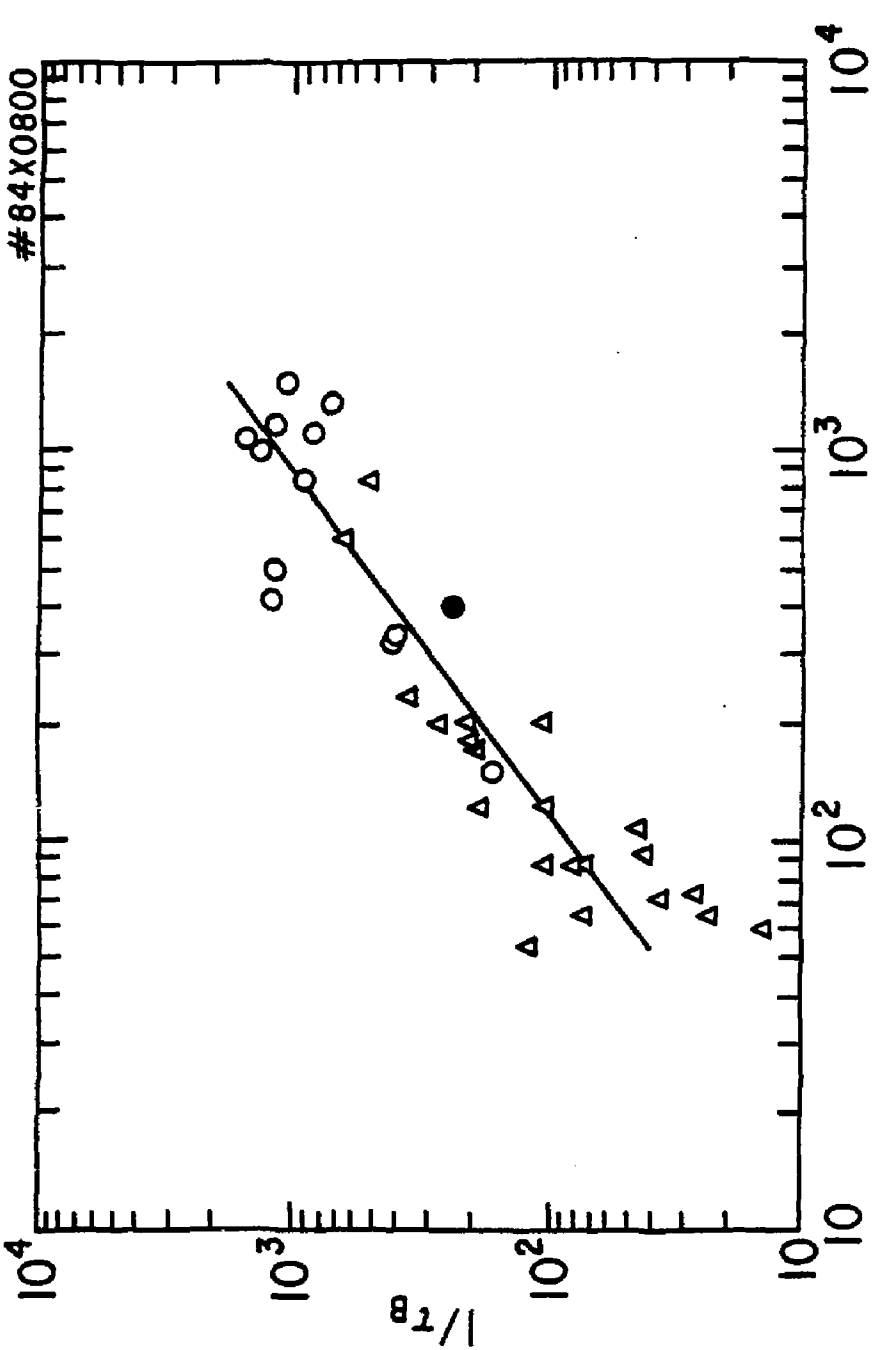

Fig. 21

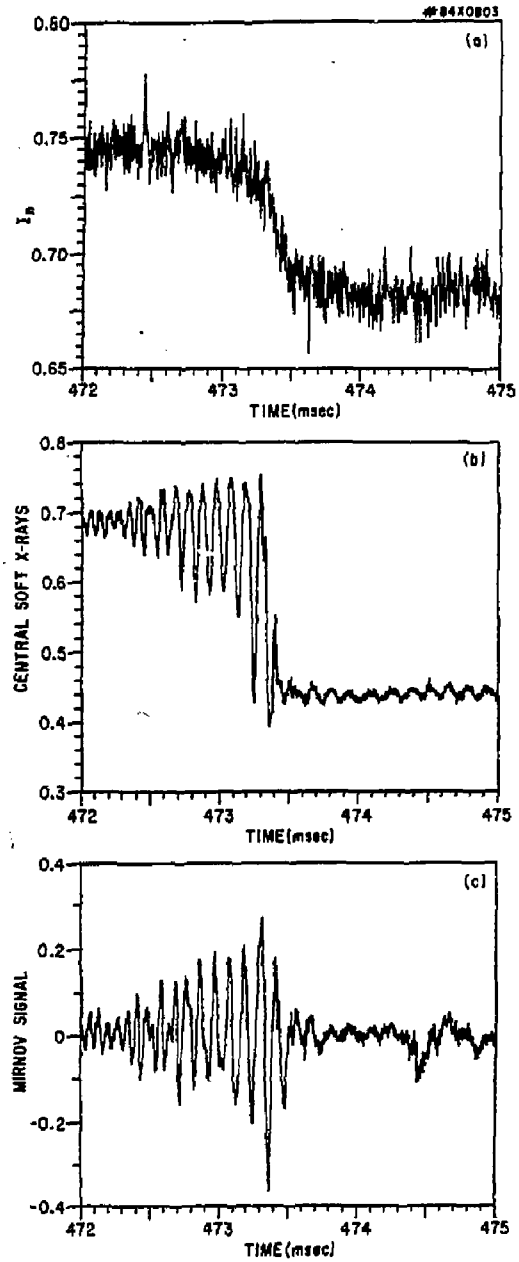
#84X0803
(a)
0.60
0.75
0.70
0.65
I_p
472
473
474
475
TIME(msec)
(b)
0.8
0.7
0.6
0.5
0.4
0.3
CENTRAL SOFT X-RAYS
472
473
474
475
TIME(msec)
(c)
0.4
0.2
0
-0.2
-0.4
MIRNOV SIGNAL
472
473
474
475
TIME(msec)

Fig. 22

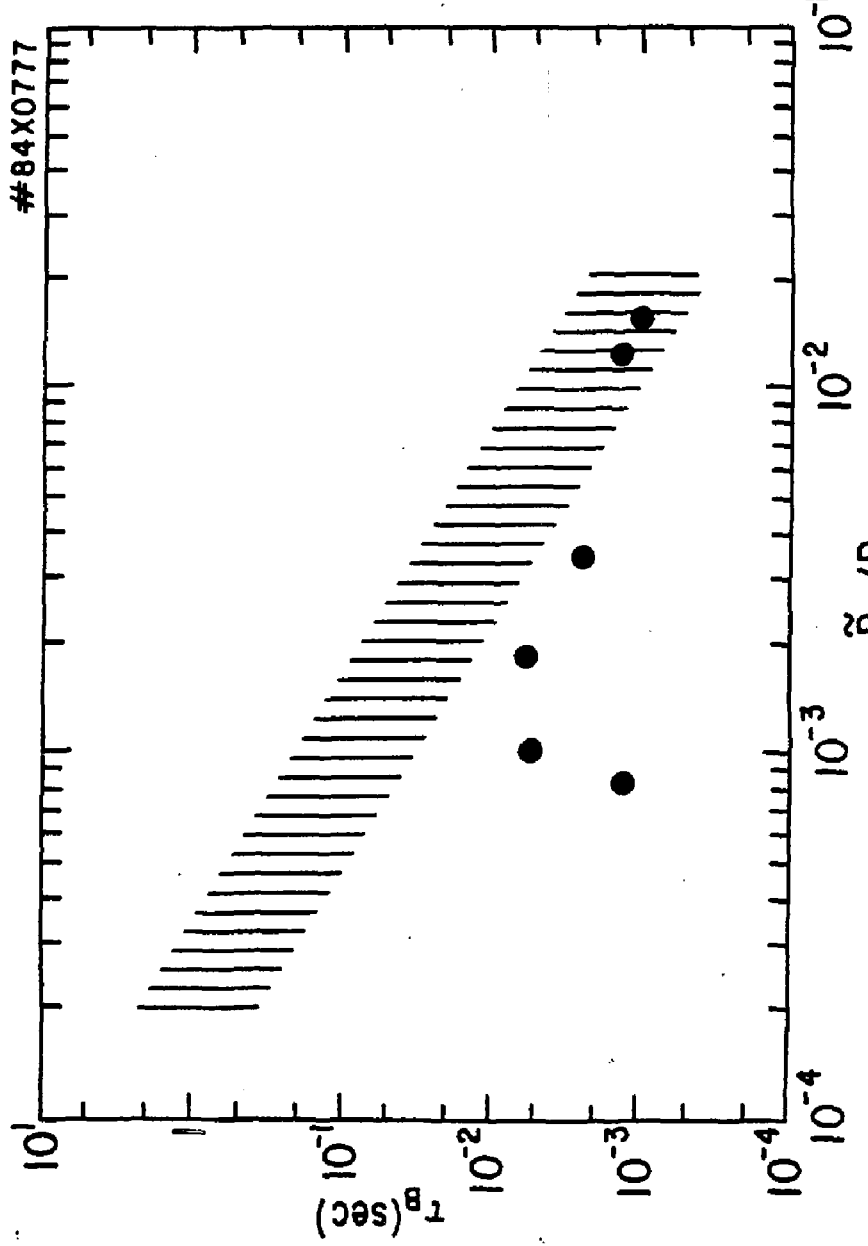
#84X0777
10^{-1}
10^{-2}
10^{-3}
10^{-4}
$\tilde{B}_\theta/B_\theta$
10^{1}
10^{-1}
10^{-2}
10^{-3}
10^{-4}
τ_B(sec)

Fig. 23

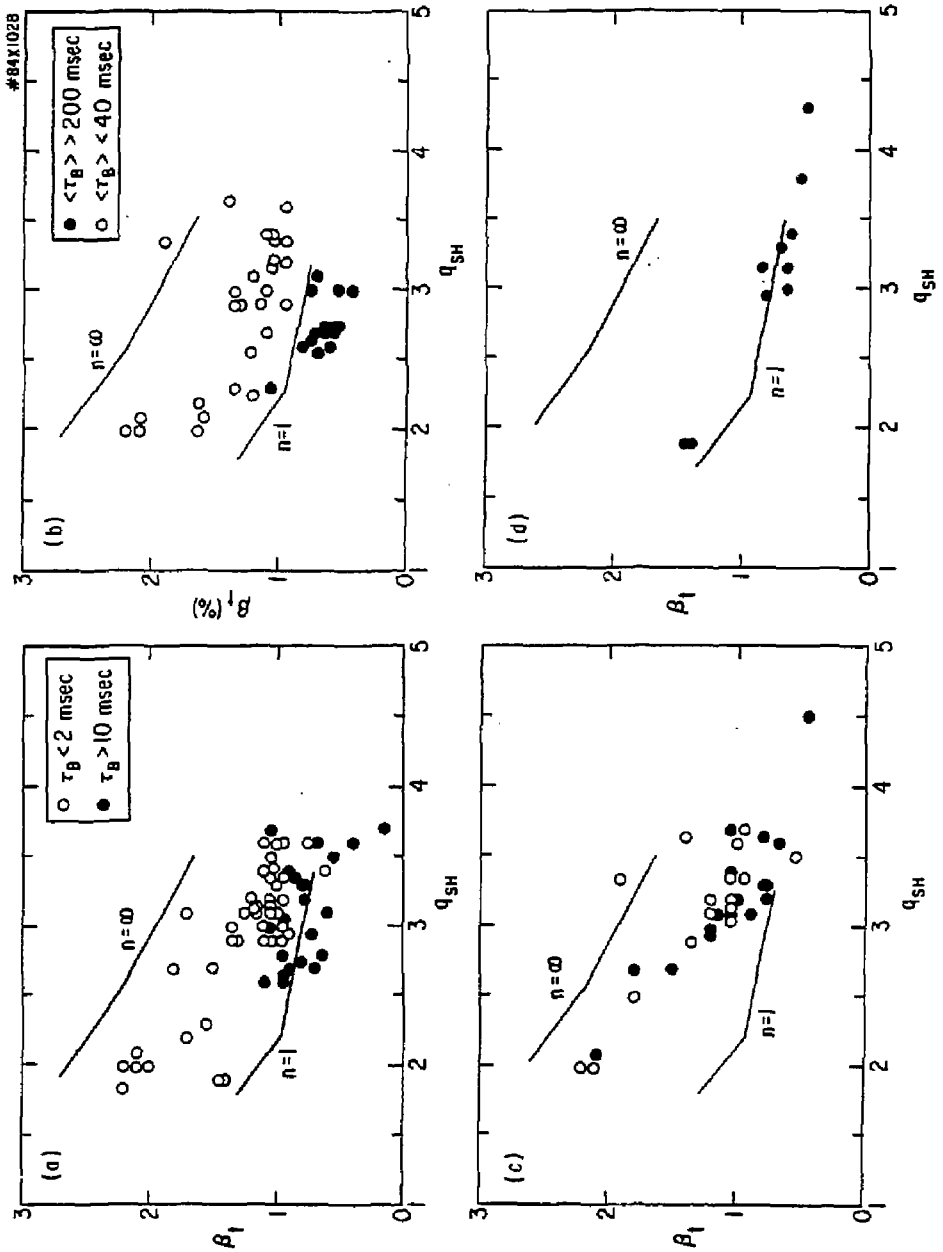
#84X1028
(a)
(b)
(c)
(d)
τ_B < 2 msec
τ_B > 10 msec
<τ_B> > 200 msec
<τ_B> < 40 msec
n=∞
n=1
β_t (%)
β_t
q_{SH}

Fig. 24

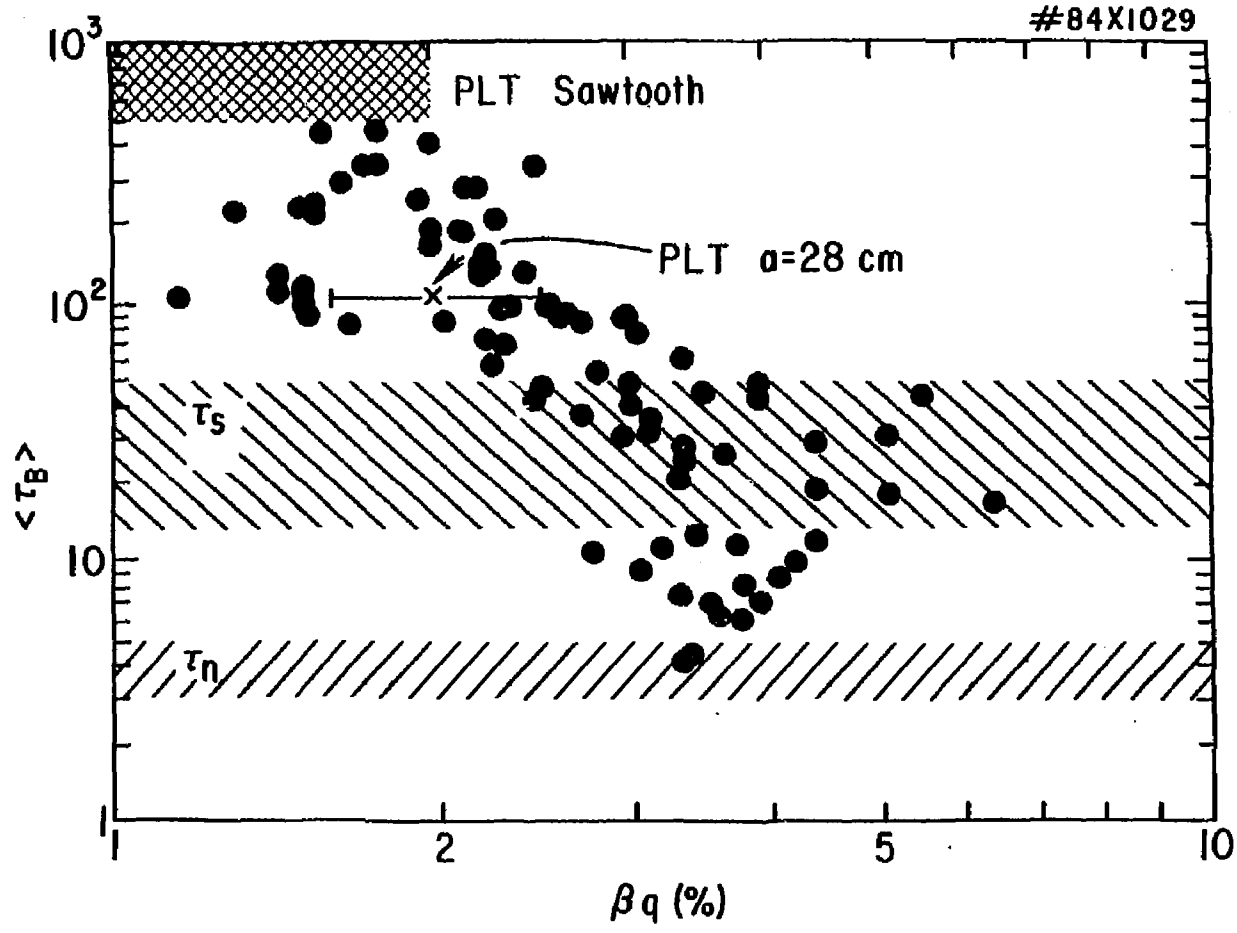
#84X1029
PLT Sawtooth
PLT a=28 cm
τ_S
τ_η
$<\tau_B>$
10^3
10^2
10
1
1
2
5
10
βq (%)

Fig. 25

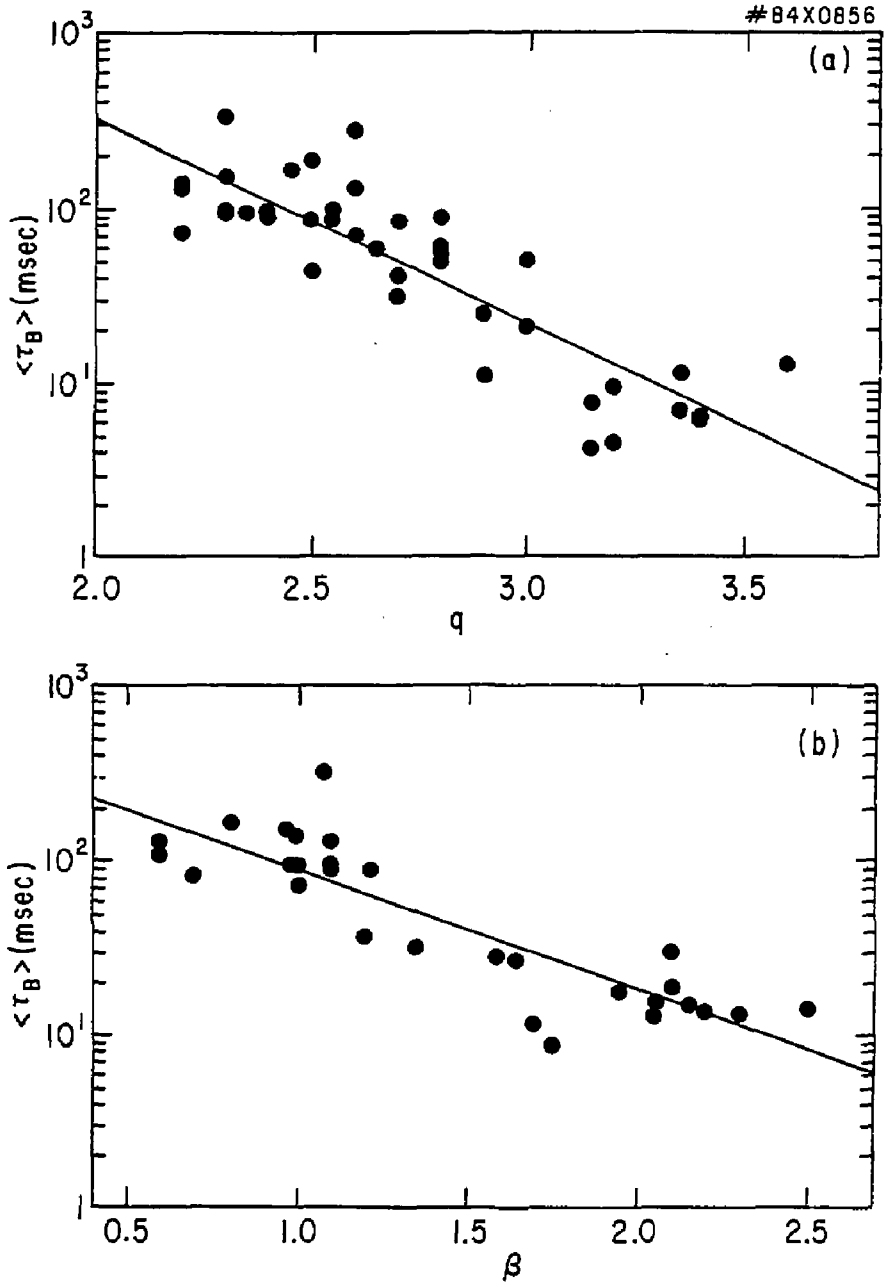
#84X0856
(a)
10^3
10^2
10^1
1
$\langle \tau_B \rangle$ (msec)
2.0
2.5
3.0
3.5
q
(b)
0.5
1.0
1.5
2.0
2.5
β

Fig. 26

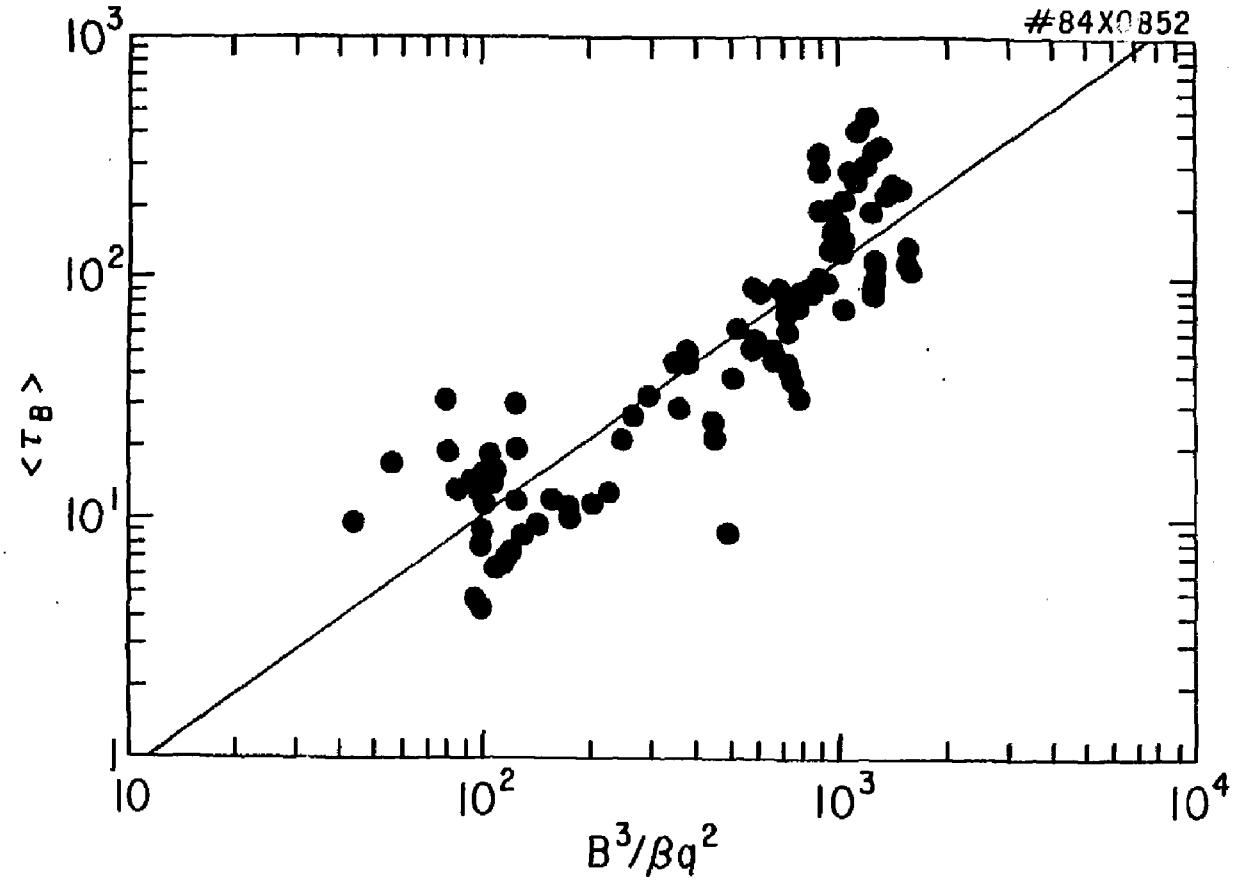
#84X0852
10^3
10^2
10^1
1
$\langle \tau_B \rangle$
10
10^2
10^3
10^4
$B^3/\beta q^2$

Fig. 27

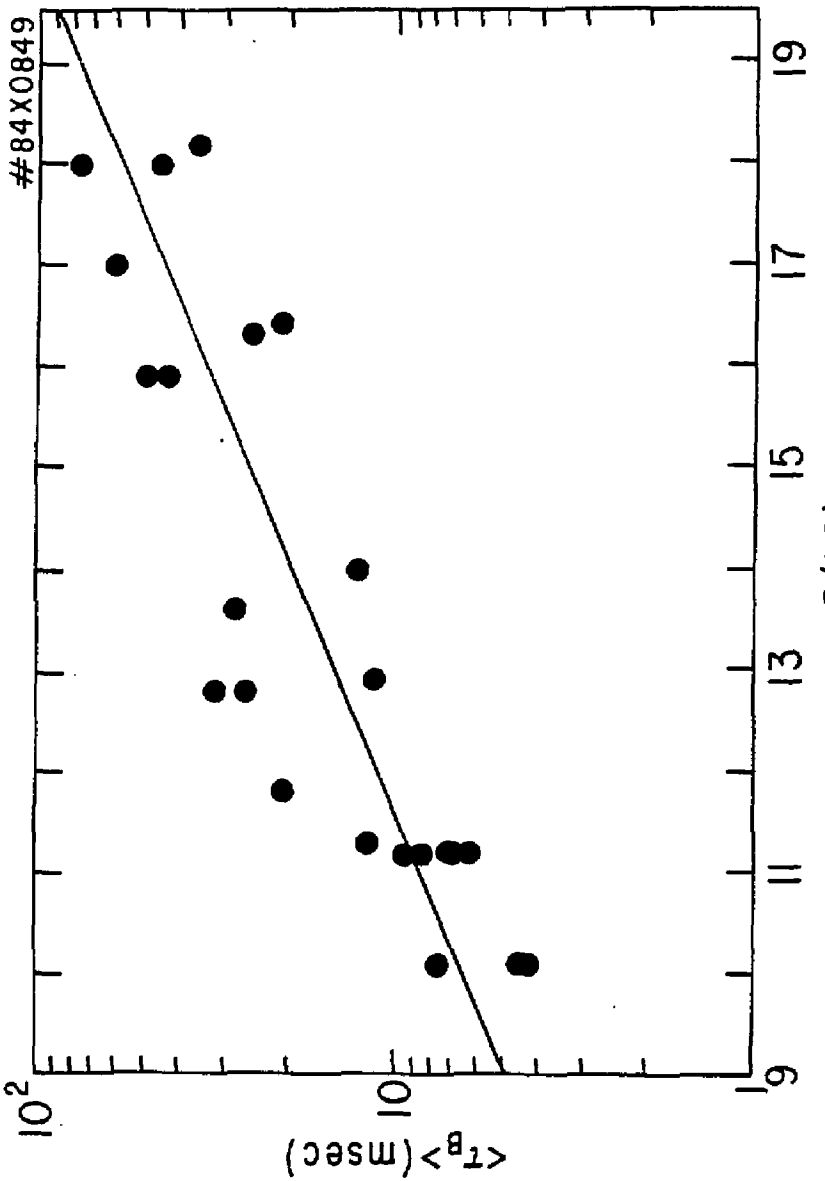

Fig. 28

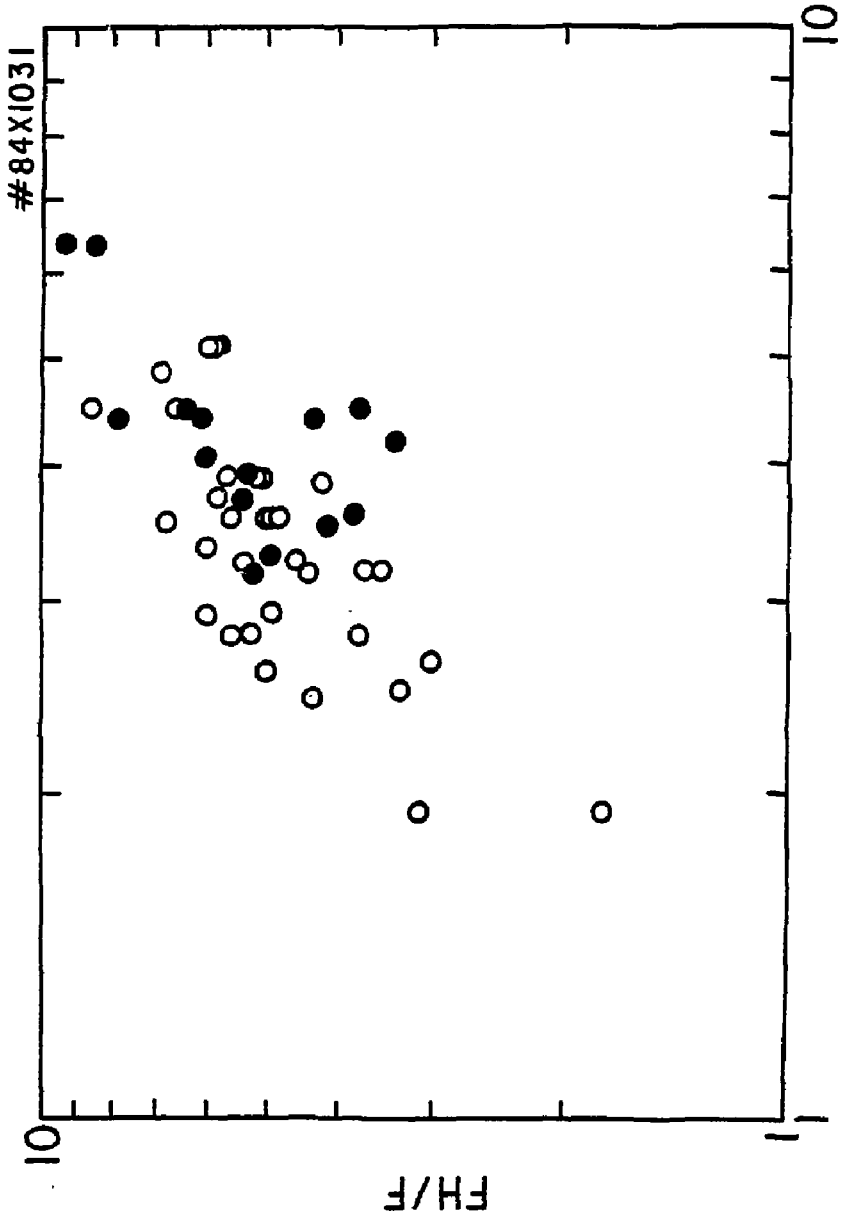

Fig. 29

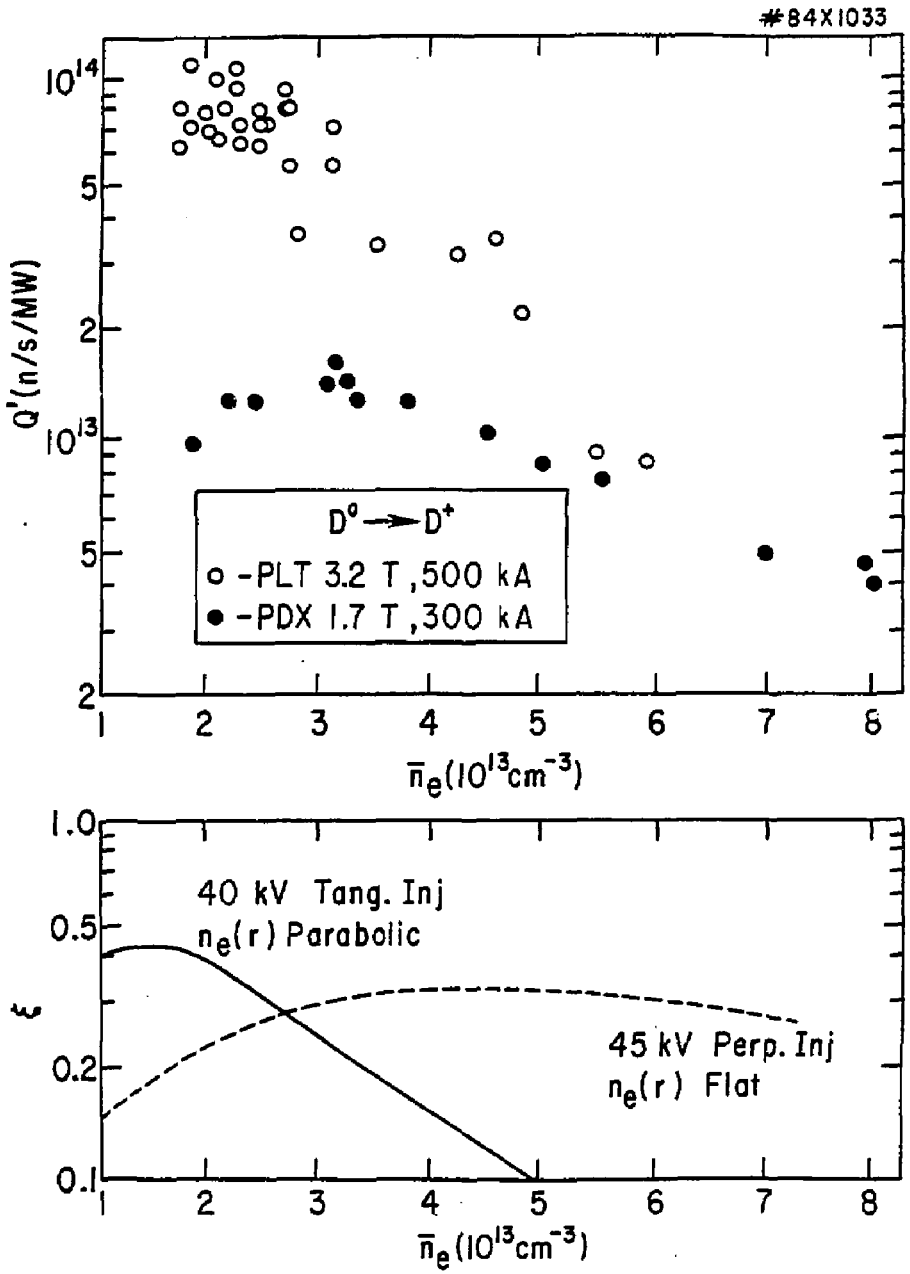
#84X1033
Q'(n/s/MW)
10^{14}
5
2
10^{13}
5
2
1 2 3 4 5 6 7 8
$\bar{n}_e(10^{13}cm^{-3})$
$D^0 \rightarrow D^+$
o -PLT 3.2 T, 500 kA
• -PDX 1.7 T, 300 kA
1.0
0.5
0.2
0.1
ξ
40 kV Tang. Inj
$n_e(r)$ Parabolic
45 kV Perp. Inj
$n_e(r)$ Flat
1 2 3 4 5 6 7 8
$\bar{n}_e(10^{13}cm^{-3})$

Fig. 30

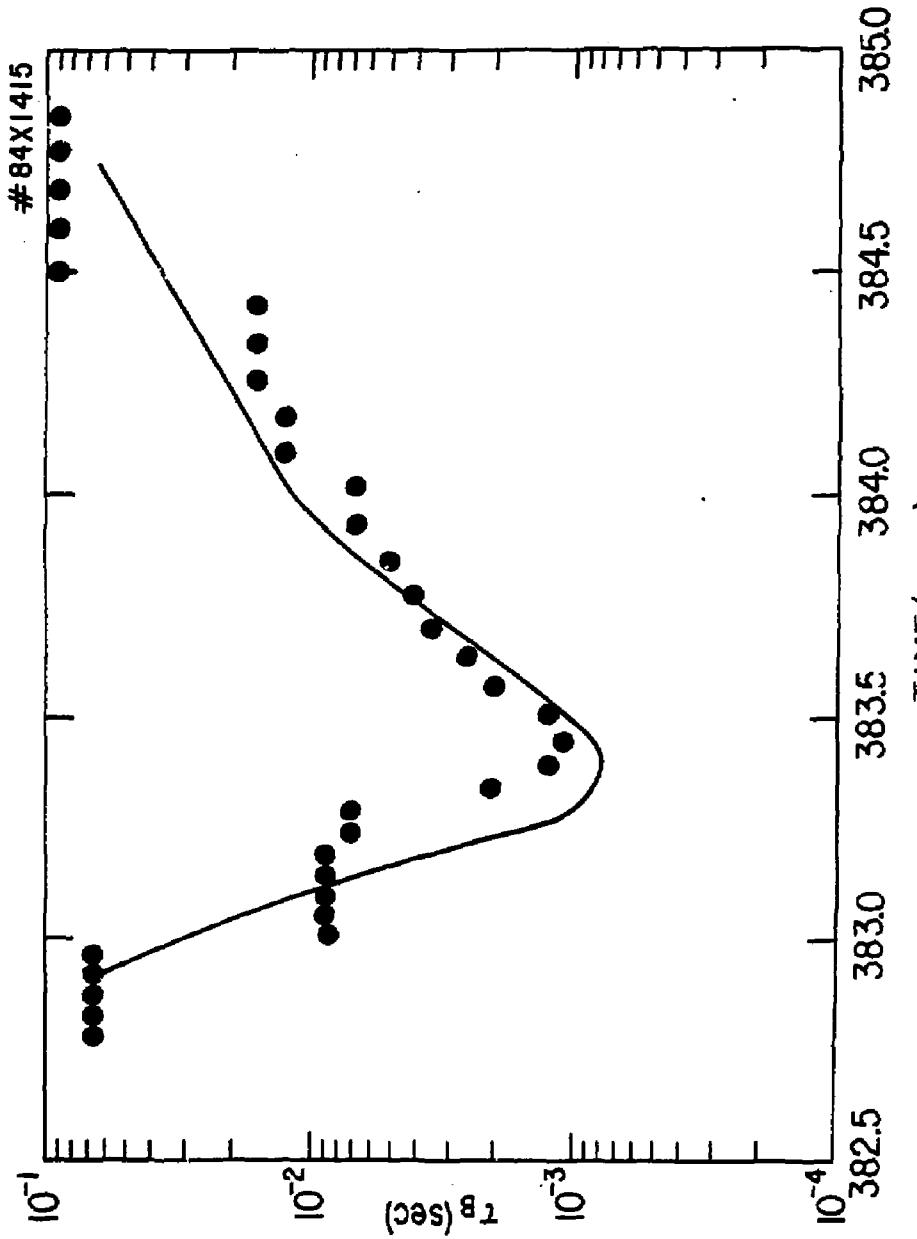
#84X1415
10^{-1}
10^{-2}
10^{-3}
10^{-4}
τ_B (sec)
382.5
383.0
383.5
384.0
384.5
385.0
TIME (msec)

Fig. 31

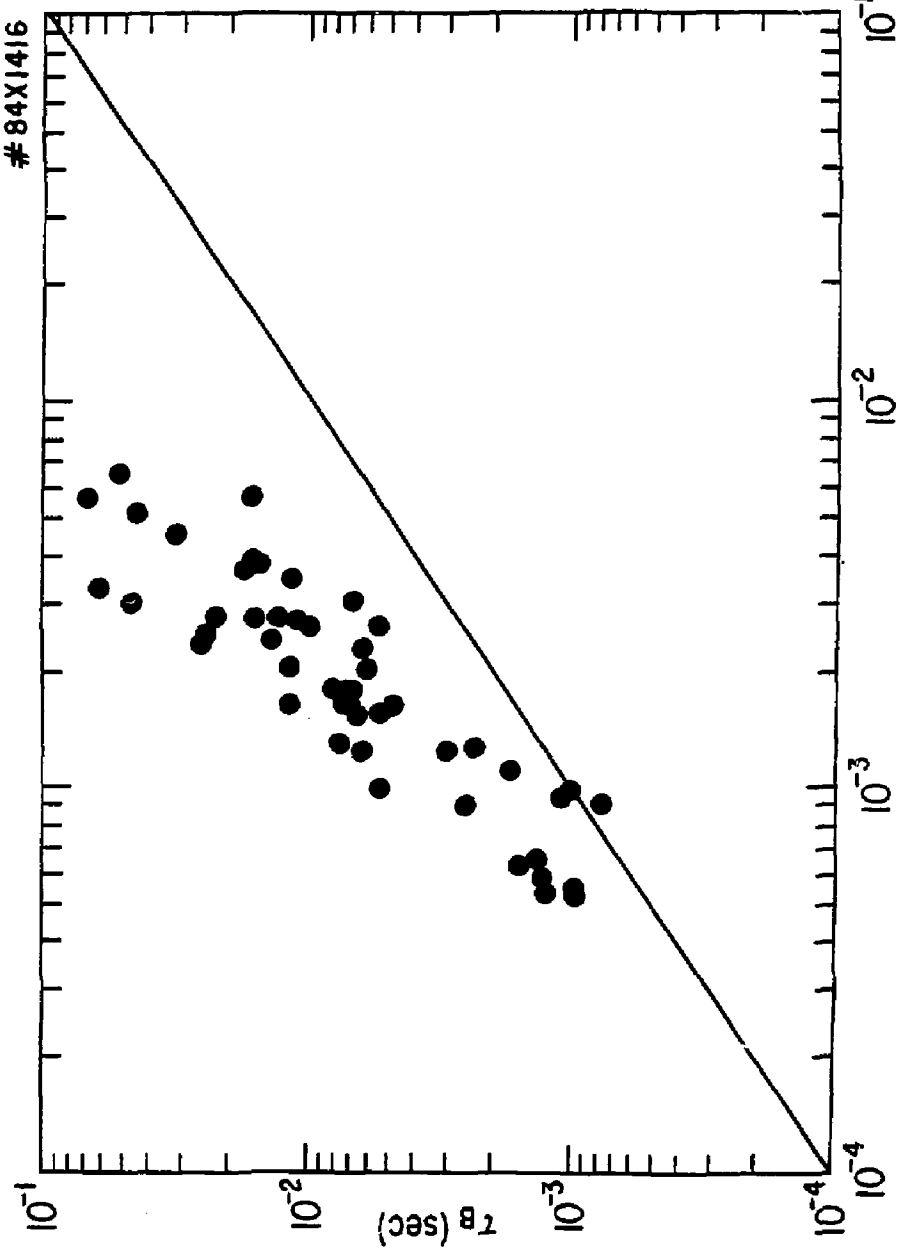

Fig. 32

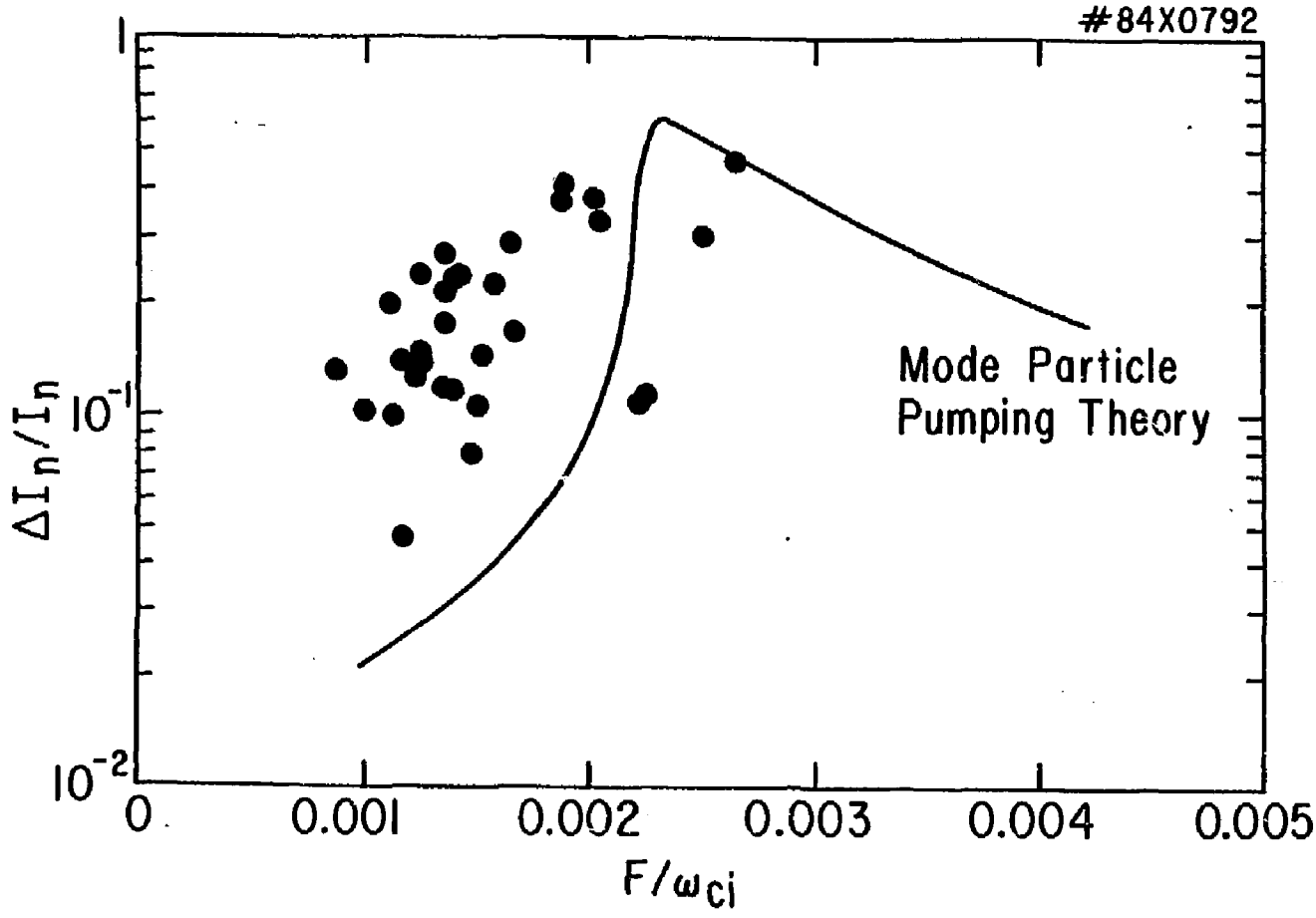
#84X0792
1
10^{-1}
10^{-2}
$\Delta I_n/I_n$
0
0.001
0.002
0.003
0.004
0.005
F/ω_{ci}
Mode Particle
Pumping Theory

Fig. 33

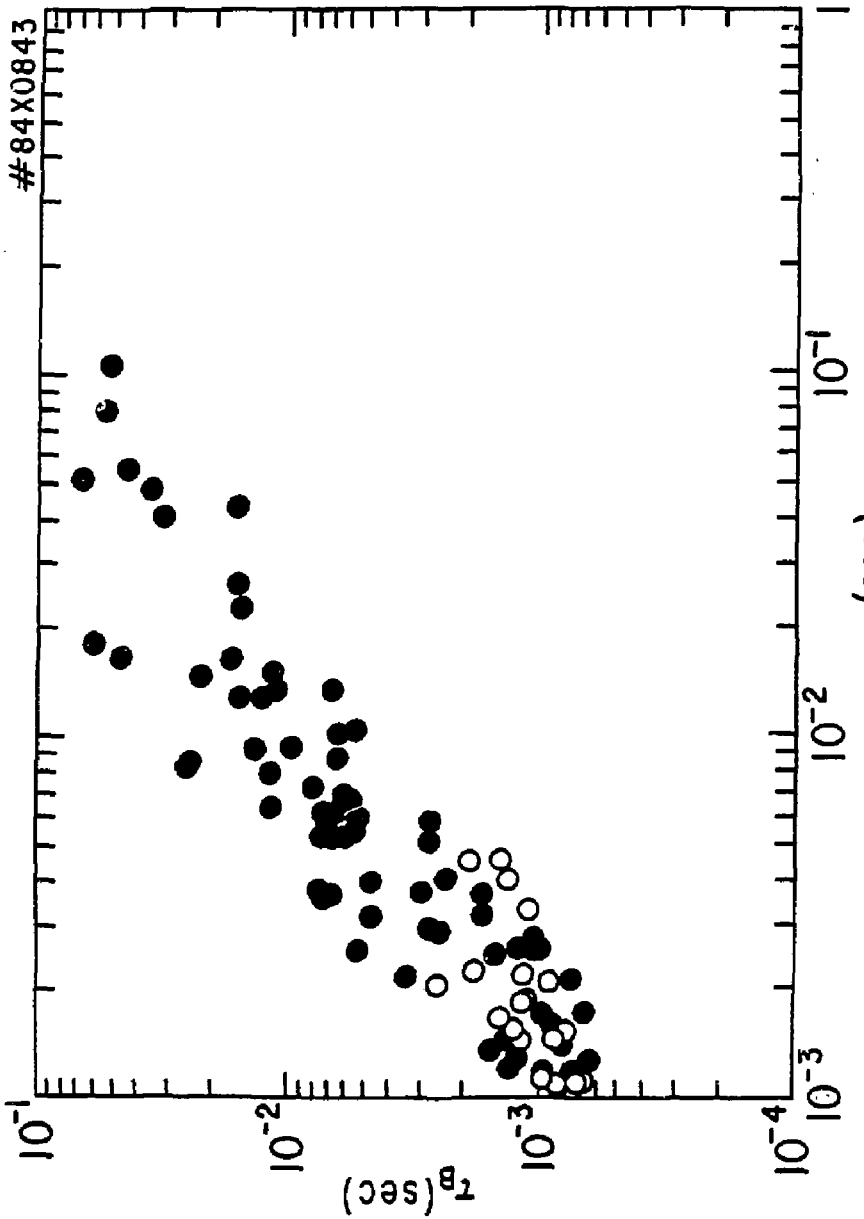

Fig. 34

EXTERNAL DISTRIBUTION IN ADDITION TO TIC UC-20

Plasma Res Lab, Austra Nat'l Univ, AUSTRALIA
Dr. Frank J. Paoloni, Univ of Wollongong, AUSTRALIA
Prof. I.R. Jones, Flinders Univ., AUSTRALIA
Prof. M.H. Brennan, Univ Sydney, AUSTRALIA
Prof. F. Cap, Inst Theo Phys, AUSTRIA
Prof. Frank Verheest, Inst theoretische, BELGIUM
Dr. D. Palumbo, Dg XII Fusion Prog, BELGIUM
Ecole Royale Militaire, Lab de Phys Plasmas, BELGIUM
Dr. P.H. Sakanaka, Univ Estadual, BRAZIL
Dr. C.R. James, Univ of Alberta, CANADA
Prof. J. Teichmann, Univ of Montreal, CANADA
Dr. H.M. Skarsgard, Univ of Saskatchewan, CANADA
Prof. S.R. Sreenivasan, University of Calgary, CANADA
Prof. Tudor W. Johnston, INRS-Energie, CANADA
Dr. Hannes Barnard, Univ British Columbia, CANADA
Dr. M.P. Bachynski, MPB Technologies, Inc., CANADA
Zhengwu Li, SW Inst Physics, CHINA
Library, Tsing Hua University, CHINA
Librarian, Institute of Physics, CHINA
Inst Plasma Phys, Academia Sinica, CHINA
Dr. Peter Lukac, Komenskeho Univ, CZECHOSLOVAKIA
The Librarian, Culham Laboratory, ENGLAND
Prof. Schatzman, Observatoire de Nice, FRANCE
J. Radet, CEN-BP6, FRANCE
AM Dupas Library, AM Dupas Library, FRANCE
Dr. Tom Muai, Academy Bibliographic, HONG KONG
Preprint Library, Cent Res Inst Phys, HUNGARY
Dr. S.K. Trehan, Panjab University, INDIA
Dr. Indra, Mohan Lal Das, Banaras Hindu Univ, INDIA
Dr. L.K. Chavda, South Gujarat Univ, INDIA
Dr. R.K. Chhajlani, Var Ruchi Marg, INDIA
P. Kaw, Physical Research Lab, INDIA
Dr. Phillip Rosenau, Israel Inst Tech, ISRAEL
Prof. S. Cuperman, Tel Aviv University, ISRAEL
Prof. G. Rostagni, Univ Di Padova, ITALY
Librarian, Int'l Ctr Theo Phys, ITALY
Miss Clelia De Palo, Assoc EURATOM-CNEN, ITALY
Biblioteca, del CNR EURATOM, ITALY
Dr. H. Tamato, Toshiba Res & Dev, JAPAN
Prof. M. Yoshikawa, JAERI, Tokai Res Est, JAPAN
Prof. T. Uchida, University of Tokyo, JAPAN
Research Info Center, Nagoya University, JAPAN
Prof. Kyoji Nishikawa, Univ of Hiroshima, JAPAN
Prof. Sigeru Mori, JAERI, JAPAN
Library, Kyoto University, JAPAN
Prof. Ichiro Kawakami, Nihon Univ, JAPAN
Prof. Setoshi Itoh, Kyushu University, JAPAN
Tech Info Division, Korea Atomic Energy, KOREA
Dr. R. England, Ciudad Universitaria, MEXICO
Bibliotheek, Fom-Inst Voor Plasma, NETHERLANDS
Prof. B.S. Liley, University of Waikato, NEW ZEALAND
Dr. Suresh C. Sharma, Univ of Calabar, NIGERIA
Prof. J.A.C. Cabral, Inst Superior Tech, PORTUGAL
Dr. Octavian Petrus, ALI CUZA University, ROMANIA
Prof. H.A. Hellberg, University of Natal, SO AFRICA
Dr. Johan de Villiers, Atomic Energy Bd, SO AFRICA
Fusion Div. Library, JEN, SPAIN
Prof. Hans Wilhelmson, Chalmers Univ Tech, SWEDEN
Dr. Lennart Stenflo, University of UMEA, SWEDEN
Library, Royal Inst Tech, SWEDEN
Dr. Erik T. Karlson, Uppsala Universitet, SWEDEN
Centre de Recherchesen, Ecole Polytech Fed, SWITZERLAND
Dr. W.L. Weise, Nat'l Bur Stand, USA
Dr. W.M. Stacey, Georg Inst Tech, USA
Dr. S.T. Wu, Univ Alabama, USA
Prof. Norman L. Oleson, Univ S Florida, USA
Dr. Benjamin Ma, Iowa State Univ, USA
Prof. Magne Kristiansen, Texas Tech Univ, USA
Dr. Raymond Askew, Auburn Univ, USA
Dr. V.T. Tolok, Kharkov Phys Tech Ins, USSR
Dr. D.D. Ryutov, Siberian Acad Sci, USSR
Dr. G.A. Eliseev, Kurchatov Institute, USSR
Dr. V.A. Glukhikh, Inst Electrophysical, USSR
Institute Gen. Physics, USSR
Prof. T.J. Boyd, Univ College N Wales, WALES
Dr. K. Schindler, Ruhr Universitat, W. GERMANY
Nuclear Res Estab, Julich Ltd, W. GERMANY
Librarian, Max-Planck Institut, W. GERMANY
Dr. H.J. Kaeppler, University Stuttgart, W. GERMANY
Bibliothek, Inst Plasmaforschung, W. GERMANY